New Approaches to Multifrequency Sp Stacking Tested in the Anatolian Region

J. Hua[1], K. M. Fischer[1], M. Wu[1] and N. A. Blom[2]

[1] Department of Earth, Environmental and Planetary Sciences, Brown University, Providence, RI 02906, USA.

[2] Bullard Laboratories, Department of Earth Sciences, University of Cambridge, Madingley Rise, Cambridge CB3 0EZ, UK.

Corresponding author: Junlin Hua (junlin_hua@brown.edu)

Key Points:

- A new approach to common conversion point stacking based on scattering kernels
- Fast and accurate quantification of the standard deviation of the weighted stack average
- Anomalously low velocity asthenosphere beneath Anatolia indicated by velocity discontinuities imaged with multifrequency data

17 **Abstract**

18 This study presents an improved approach to common-conversion point stacking of converted

19 body waves that incorporates scattering kernels, accurate and efficient measurement of stack

20 uncertainties, and an alternative method for estimating free surface seismic velocities. To better

21 separate waveforms into the P and SV components to calculate receiver functions, we developed

22 an alternative method to measure near surface compressional and shear wave velocities from

23 particle motions. To more accurately reflect converted phase scattering kernels in the common-

24 conversion point stack, we defined new weighting functions to project receiver function

25 amplitudes only to locations where sensitivies to horizontal discontinuities are high. To better

26 quantify stack uncertainties, we derived an expression for the standard deviation of the stack

27 amplitude that is more efficient than bootstrapping and can be used for any problem requiring the

28 standard deviation of a weighted average. We tested these improved methods on Sp phase data

29 from the Anatolian region, using multiple bandpass filters to image velocity gradients of varying

30 depth extents. Common conversion point stacks of 23,787 Sp receiver functions demonstrate that

31 the new weighting functions produce clearer and more continuous mantle phases, compared to

32 previous approaches. The stacks reveal a positive velocity gradient at 80-150 km depth that is

33 consistent with the base of an asthenospheric low velocity layer. This feature is particularly

34 strong in stacks of longer period data, indicating it represents a gradual velocity gradient. At

35 shorter periods, a lithosphere-asthenosphere boundary phase is observed at 60-90 km depth,

36 marking the top of the low velocity layer.

37

38

39 **Plain Language Summary**

40 This paper presents a new method that more accurately incorporates the physics of seismic

41 scattering into how the wave records are combined to form images of gradients in seismic

42 velocity structure. This method was tested on data from the Anatolian region, where the

43 asthenosphere is known to have low seismic wave velocities, consistent with high mantle

44 temperatures and possibly small fractions of partial melt, as suggested by the presence of

45   volcanic fields at the surface. However, the depth of the asthenospheric low velocity layer is not

46   well known. In this study, we locate this low velocity mantle layer by applying the newly

47   developed imaging method to seismic shear waves that convert to compressional waves at the

48   velocity gradients that mark the layer boundaries. This study is the first to clearly resolve both

49   the lower and upper margins of the asthenosphere for the whole region. The top of the layer

50   corresponds to the lithosphere-asthenosphere boundary at 60-90 km depth, and this velocity

51   gradient is localized in depth. However, the bottom boundary, which lies at depths of 80-150 km,

52   occurs over a broader depth range.

53

54   1. Introduction

55   Teleseismic body waves that convert from S to P vibration (or vice versa) at velocity or density

56   anomalies are potent tools for imaging velocity discontinuities in the crust and mantle. To

57   isolate the effects of Earth structure, incident phases are often deconvolved from converted

58   phases to remove source and instrument information, resulting in receiver functions (e.g. Farra &

59   Vinnik, 2000) for Ps (incident P wave with converted S wave) and Sp (incident S wave with

60   converted P wave) phases.

61   Common-conversion point (CCP) stacking of receiver functions (e.g. Dueker & Sheehan, 1997)

62   is often used to image mantle discontinuities. During CCP stacking, converted waves are

63   assumed to be generated around converted wave ray paths. Receiver function amplitudes

64   recorded at surface stations are projected back along the paths, and the image is constructed by

65   summing receiver function amplitudes as a function of position, assuming spatial functions that

66   weight how a receiver function on a particular ray path contributes to the summed amplitude at a

67   given location. In prior studies, these spatial functions are either represented by geographic bins

68   of conversion points (e.g. Dueker & Sheehan, 1997; Kind et al., 2012; Rondenay, 2009), or by

69   empirically defined weighting functions that represent Fresnel zones for vertically incident

70   waves (e.g. Lekić & Fischer, 2017; Lekic et al., 2011; Wittlinger & Farra, 2007). However, to

71   incorporate the physics of wave scattering into CCP stacking, these spatial functions should be

72   consistent with the sensitivity kernels that describe how scattering from a point on a velocity

73   discontinuity contributes to an observed converted phase, for example the scattering kernels for

74   Sp and Ps phases(e.g. Bostock & Rondenay, 1999; Bostock et al., 2001; Hansen & Schmandt,

75   2017; Hua et al., 2020; Mancinelli & Fischer, 2017). This condition is typically not met in prior

76   CCP stacking approaches. Therefore, a new CCP stacking scheme is developed here based on

77   the shape of scattering kernels while assuming that velocity structure is laterally invariant

78   (Section 2.2).

79   High quality receiver functions are an essential ingredient of CCP stacking, and accurate incident

80   and converted waveform components are necessary for robust receiver functions. While some

81   studies deconvolve vertical from radial components to represent Ps receiver functions (e.g. Zor et

82   al., 2003), others deconvolve P from SV. However, for Sp receiver functions, deconvolution of

83   SV from P is necessary, due to the more horizontal incidence of Sp phases at the station (e.g.

84   Kind et al., 2012). P and SV components are sometimes approximated using rotation of radial

85   and vertical components into a ray-parallel and ray-normal reference frame (Kind et al., 2012),

86   but, because the recorded seismogram is a combination of incident and reflected waves, other

87   studies calculate P and SV components using the free-surface transform of Kennett (1991) (e.g.

88   Abt et al., 2010; Bostock & Rondenay, 1999). This latter approach is more accurate in isolating

89   incident and converted waveform components, but it requires values for near surface P and S

90   velocities. Building on prior approaches (Abt et al., 2010; Park and Ishii, 2018) this study

91   introduces a new method to accurately measure near surface P and S velocities from P and S

92   particle motions in Section 2.1.

93   Accurate quantification of uncertainties in CCP stack amplitudes are critical to evaluating which

94   features are robust and avoiding over-interpretation. The uncertainty is often quantified by the

95   standard deviation of the stacked receiver function amplitude, for example as measured by

96   bootstrapping (Hopper et al., 2014). During bootstrapping, individual receiver functions are

97   randomly resampled and CCP stacked over multiple iterations, and the standard deviation of

98   amplitude at each point among the multiple CCP stacks is calculated. However, this process is

99   computationally expensive. In this study we derived a theoretical expression for accurately

100   measuring the standard deviation of any weighted average and applied this to CCP stacking

101   (Section 2.3), thus avoiding the need for bootstrapping.

102   These methodological improvements were tested by applying Sp receiver function CCP stacking

103   to the upper mantle beneath the Anatolian region (Figure 1). Sp receiver functions were

104   employed because they are not contaminated by crustal reverberations which affect Ps receiver

105   functions in the time window where scattered waves from the shallow upper mantle arrive (Kind

106   et al., 2012; Yuan et al., 2006). In addition, as will be shown in Section 2.2, the sensitivity

107   kernels for Sp receiver functions are more effective at imaging quasi-horizontal upper mantle

108   discontinuities with CCP stacking, particularly for the station spacing available in Anatolia

109   (Figure 1).

110   The Anatolian region lies within the Alpine-Himalayan orogenic belt. In eastern Anatolia,

111   collision between the Arabian and Eurasian plates began in the Oligocene, while central and

112   western Anatolia have been escaping westwards, with their ongoing motion accommodated by

113   the North Anatolian fault zone and the East Anatolian fault zone (e.g. Jolivet et al., 2013;

114   Reilinger et al., 2006; Schildgen et al., 2014; A. M. C. Şengör et al., 2008). Numerous seismic

115   models based on tomography with varied seismic phases have found thin lithosphere and low

116   velocity asthenosphere beneath Anatolia, with particularly low velocities beneath eastern

117   Anatolia; many models also contain dipping high velocity anomalies that have been interpreted

118   as fragments of subducted lithosphere, with zones of lower velocity asthenosphere flowing

119   between them (Bakırcı et al., 2012; Berk Biryol et al., 2011; Blom et al., 2020; Delph et al.,

120   2015; Fichtner et al., 2013; Gans et al., 2009; Govers & Fichtner, 2016; Portner et al., 2018;

121   Salaün et al., 2012; Wei et al., 2019; H. Zhu, 2018). Seismic models are typically consistent with

122   the view that slab detachment occurred earlier beneath eastern Anatolia, creating a broad window

123   filled with hot asthenosphere and surface uplift (Faccenna et al., 2006; Govers & Fichtner, 2016;

124   Keskin, 2003; Schildgen et al., 2014; A. Şengör et al., 2003). Slab fragmentation and

125   asthenospheric influx subsequently propagated west, contributing to uplift in central Anatolia

126   (McNab et al., 2018; Schildgen et al., 2014).   The particularly low velocity asthenosphere

127   beneath eastern Anatolia is consistent with elevated mantle potential temperatures inferred from

128   geochemical data (e.g. McNab et al., 2018; Nikogosian et al., 2018; Reid et al., 2017).

129   Constraints on seismic velocity interfaces from converted body waves have also illuminated the

130   properties of the Anatolian crust and mantle. Numerous studies have focused on crustal

131   properties (e.g. Abgarmi et al., 2017; Frederiksen et al., 2015; Karabulut et al., 2019; Licciardi et

132   al., 2018; Ozacar et al., 2008; Vanacore et al., 2013; L. Zhu et al., 2006; Zor et al., 2003).

133   However, two prior studies used Sp phases to image mantle discontinuities. Angus et al. (2006)

134   found Sp phases consistent with a decrease in velocity over the lithosphere-asthenosphere

135   boundary (LAB) at depths of 60-80 km in eastern Anatolia, whereas Kind et al. (2015) inferred

136   LAB velocity gradients at 80-100 km across Anatolia. In this study, we re-visit Sp CCP stacking

137   in the Anatolian mantle, enhanced by the methodological improvements described above and

138   additional data, to refine constraints on lithospheric thickness and to search for mantle

139   discontinuities associated with the base of the asthenosphere.

140   We first introduce the new method improvements (Section 2) and then describe the full process

141   of data acquisition, processing and calculation of the CCP stack (Section 3). Key operations

142   within each step of this process are briefly summarized in Figure 2. Results from the application

143   of these methods to the Anatolian region, including the observation of an unusually strong

144   positive velocity gradient at depths of 80-150 km, are discussed in Section 4.

145

2. Method Improvements

147   2.1. Free-surface Velocities and P-SV Phase Separation

148   The Sp receiver functions used in this study rely on accurate calculation of P and SV components

149   from radial and vertical components based on a free-surface transform (Kennett, 1991) that

150   removes the effect of free-surface reflection. The transform is expressed as

151
$$
\begin{pmatrix} P \\ SV \end{pmatrix} = \mathbf{T}(\alpha^{FS}, \beta^{FS}, p) \begin{pmatrix} R \\ Z \end{pmatrix}, \quad \mathbf{T} = \begin{pmatrix} \dfrac{p(\beta^{FS})^2}{\alpha^{FS}} & \dfrac{(\beta^{FS})^2 p^2 - 0.5}{\alpha^{FS} q_\alpha} \\ \dfrac{0.5 - (\beta^{FS})^2 p^2}{\beta^{FS} q_\beta} & p\beta^{FS} \end{pmatrix},
$$
(1)

152   where R and Z are the recorded vertical and the radial components, P and SV are P and SV

153   components before encountering the free-surface, $\mathbf{T}$ is the free-surface transform matrix, α^{FS}

154   and β^{FS} are the assumed near-surface compressional velocity (V$_p$) and shear velocity (V$_s$), p is

155   the ray parameter at the station in s/km, and $q_\alpha = [(\alpha^{FS})^{-2} - p^2)]^{0.5}$, $q_\beta = [(\beta^{FS})^{-2} - p^2)]^{0.5}$.

156   Therefore, accurate estimation of α^{FS} and β^{FS} is required to perform the transform correctly.

157   Previously, Abt et al. (2010) also used equation (1) to obtain P and SV components for receiver

158   function calculations, and they determined the free-surface velocities by performing a grid search

159   over α^{FS} and β^{FS} using equation (1) to minimize SV in the P arrival window and P in the S

160   arrival window. However, this method does not use the information in P for the P arrival, and

161   information in SV for the S arrival. Other studies have investigated the free surface behavior of

162   the polarization of the recorded phase (Wiechert & Zoeppritz, 1907) to better constrain α^{FS} and

163   β^{FS} (Park & Ishii, 2018), and have used the frequency-dependence of the polarization to

164   constrain local velocity stratification (Hannemann et al., 2016; Park et al., 2019; Svenningsen &

165   Jacobsen, 2007). In this study, a new method is developed for estimating free-surface velocities.

166   This method incorporates the behavior of P and SV at the free surface, including free surface

167   reflections, but is not based on direct measurement of polarizations.

168   If the true P and SV components are expressed as P_0 and SV_0, and the true V_p and V_s are α_0^{FS}

169   and β_0^{FS}, the recorded R and Z can be expressed as

170    $$\begin{pmatrix} R \\ Z \end{pmatrix} = \mathbf{R}(\alpha^{FS} = \alpha_0^{FS}, \beta^{FS} = \beta_0^{FS}, p)\begin{pmatrix} P_0 \\ SV_0 \end{pmatrix}, \quad \mathbf{R} = \frac{1}{q_\gamma^4 + 4p^2 q_\alpha q_\beta}\begin{pmatrix} \dfrac{4p\alpha^{FS}q_\alpha q_\beta}{(\beta^{FS})^2} & \dfrac{2q_\gamma^2 q_\beta}{\beta} \\ -\dfrac{2\alpha^{FS}q_\gamma^2 q_\alpha}{(\beta^{FS})^2} & \dfrac{4pq_\alpha q_\beta}{\beta} \end{pmatrix}, \quad (2)$$

171   where $q_\gamma = [(\beta^{FS})^{-2} - 2p^2)]^{0.5}$, and $\mathbf{R}$ is the reflection matrix containing reflection coefficients

172   at the free surface (e.g. Aki & Richards, 2002), which is also the inverse matrix of $\mathbf{T}$. By

173   substituting equation (2) into (1), the transformed P and SV components can be expressed as

174    $$\begin{pmatrix} P \\ SV \end{pmatrix} = \mathbf{T}(\alpha^{FS}, \beta^{FS}, p)\mathbf{R}(\alpha_0^{FS}, \beta_0^{FS}, p)\begin{pmatrix} P_0 \\ SV_0 \end{pmatrix}. \quad (3)$$

175   With equation (3), to solve for α_0^{FS} and β_0^{FS}, three particle motion patterns

176
$$\mathbf{C}_1(\alpha^{FS},\beta^{FS}) = \frac{P \cdot SV}{R \cdot Z}, \quad \mathbf{C}_2(\alpha^{FS},\beta^{FS}) = \frac{P \cdot P}{R \cdot Z} \quad \text{and} \quad \mathbf{C}_3(\alpha^{FS},\beta^{FS}) = \frac{SV \cdot SV}{R \cdot Z} \qquad (4)$$

177   are first measured for both P and S arrivals (e.g. Figure 3). Specifically, P and SV are

178   calculated from equation (1) for different α^{FS} (2.7-8.1 km/s with a 0.03 km/s increment) and

179   β^{FS} (1.5-4.5 km/s with a 0.0167 km/s increment), and the patterns are then calculated using

180   equation (4), making the observed patterns functions of α^{FS} and β^{FS}. The patterns include

181   scaling by $R \cdot Z$ to normalize the amplitude of the patterns, so that the amplitude of the

182   waveform does not affect the results. For the case of a half space with V_p=4.92 km/s and V_s=2.82

183   km/s and a P wave with a ray parameter of 0.0482 s/km, the three patterns based on propagator

184   matrix synthetic seismograms (Keith & Crampin, 1977) are shown in Figures 3a to 3c, and the

185   patterns for an SV wave with a ray parameter 0.1098 s/km are shown in Figures 3e to 3g.

186   After obtaining patterns from the observed waveforms, P and SV are then predicted for

187   different α_0^{FS} and β_0^{FS} with equation (3) by setting $SV_0 = 0$ for the P arrival and $P_0 = 0$ for the S

188   arrival, assuming the ray parameter of the real waveform. With the predicted P and SV, the

189   three predicted patterns are calculated according to equation (4) and are labelled as $\mathbf{C}_1^P$, $\mathbf{C}_2^P$ and

190    $\mathbf{C}_3^P$. The predicted patterns are not only functions of α^{FS} and β^{FS} but also α_0^{FS} and β_0^{FS}.

191   Optimal α_0^{FS} and β_0^{FS} values are then obtained by matching $\mathbf{C}_1^P$, $\mathbf{C}_2^P$ and $\mathbf{C}_3^P$ for different α_0^{FS}

192   and β_0^{FS} to $\mathbf{C}_1$, $\mathbf{C}_2$ and $\mathbf{C}_3$.

193   In practice, instead of using P and S arrivals together to constrain α_0^{FS} and β_0^{FS}, α_0^{FS} is obtained

194   from S arrival pattern matching, and β_0^{FS} from P arrival pattern matching (Figures 3d & 3h).

195   This choice is motivated by the fact that the P arrival polarization does not depend on α_0^{FS}, a

196   result also shown in Park and Ishii (2018), and therefore the P arrival $\mathbf{C}_1$, $\mathbf{C}_2$ and $\mathbf{C}_3$ patterns

197   also do not depend on α_0^{FS}. While the value of $\mathbf{C}_2$ does vary with α^{FS} in the P arrival $\mathbf{C}_2$

198   pattern (Figure 3b), the $\mathbf{C}_2$ pattern itself does not vary with values of α_0^{FS}. The independence of

199   the P arrival $\mathbf{C}_1$, $\mathbf{C}_2$ and $\mathbf{C}_3$ patterns can be demonstrated as follows. From equations (1) and

200   (4), it can be shown that the $\mathbf{C}_1$, $\mathbf{C}_2$ and $\mathbf{C}_3$ patterns depend only on the polarization R/Z, and

201   from equation (2), the polarization is expressed as

$$\frac{R}{Z} = \frac{\mathbf{R}_{11}P_0 + \mathbf{R}_{12}SV_0}{\mathbf{R}_{21}P_0 + \mathbf{R}_{22}SV_0}, \tag{5}$$

203   where the subscripts refer to the row and column of an element in the $\mathbf{R}$ matrix. For the P

204   arrival, $SV_0 = 0$, and the polarization $R/Z = -2pq_\beta/q_\gamma^2$ (equations 2 & 5). Therefore, the

205   polarization is independent of α_0^{FS}. For the S arrival, $P_0 = 0$, and the polarization is equal to

206    $q_\gamma^2/2pq_\alpha$ (equations 2 & 5), which depends on both α_0^{FS} and β_0^{FS}.

207   In practice, using P arrival patterns, a uniform grid search is performed over β_0^{FS}, with 181

208   values that range from 1.5 km/s to 4.5 km/s, to find the value that minimizes a misfit function

209   defined as

$$\text{misfit} = \sqrt{\left\|\mathbf{C}_1 - \mathbf{C}_1^P\right\|_2^2 + \left\|\mathbf{C}_2 - \mathbf{C}_2^P\right\|_2^2 + \left\|\mathbf{C}_3 - \mathbf{C}_3^P\right\|_2^2}, \tag{6}$$

211   where the L_2-norm refers to the norm of a vector (i.e. treating $\mathbf{C}_1$ as a vector with 181×181

212   elements). We then use the β_0^{FS} value from this step together with the S arrival patterns to obtain

213   α_0^{FS} by minimizing the same misfit function in equation (6), but through a grid search over α_0^{FS}

214   with a minimum value of 2.7 km/s and a maximum value of 8.1 km/s.

215   This approach differs from that of Park and Ishii (2018) in two significant ways. First, Park and

216   Ishii (2018) solve for free-surface velocities based on minimizing misfits between observed and

217   predicted P incidence angles and S polarizations. In contrast, we minimize misfits between

218   observed and predicted $\mathbf{C}$ patterns (equation 6), which are the normalized dot products of P and

219   SV particle motions (equation 4). Second, Park and Ishii (2018) solve for free-surface P and S

220   velocities simultaneously, while we first use equation (4) with P arrival data to solve for β_0^{FS}

221   and then, with fixed β_0^{FS}, use equation (4) with S arrival data to solve for α_0^{FS}. Advantages of

222   using only the P arrival patterns to solve for β_0^{FS} are that P phases typically have much higher

223   signal-to-noise ratios than S phases, and trade-offs between α_0^{FS} and β_0^{FS} are to some extent

224   reduced since P arrival patterns do not depend on α_0^{FS}.

225   The synthetic example in Figure 3 demonstrates the effectiveness of the pattern-matching

226   method in finding α_0^{FS} and β_0^{FS}. For the grid search over β_0^{FS} using the P arrival, the estimated

227   value of β_0^{FS} matches the free surface V_s from the model used to generate the synthetics (Figure

228   3d). In addition, while all the misfit components are minimized at the same value of β_0^{FS}, the $\mathbf{C}_2$

229   misfit dominates the total misfit relative to $\mathbf{C}_1$ and $\mathbf{C}_3$. This finding shows the advantage of the

230   new method over the approach in Abt et al. (2010) which relied only on $\mathbf{C}_1$. For the S arrival,

231   the grid search over α_0^{FS} yields a minimum misfit α_0^{FS} that matches V_p in the input model

232   (Figure 3h). However, in this case $\mathbf{C}_1$, $\mathbf{C}_2$ and $\mathbf{C}_3$ all have substantial contributions to the total

233   misfit, which again emphasizes the importance of using use all the patterns instead of relying

234   only on $\mathbf{C}_1$ as in Abt et al. (2010).

235   To obtain free-surface velocities from multiple events at a single station, we first weight the

236   velocity estimates by a value the describes the quality of the seismic phase, and then take the

237   weighted mean of estimates for the station. One quality factor is a signal-to-noise ratio measured

238   with moving signal and noise windows applied to the envelope function of Z for P arrivals, and

239   to the envelope function of R for S arrivals. Signal-to-noise is defined as the average amplitude

240   in the 5 s signal window divided by the average amplitude in the 20 s noise window, and the

241   signal-to-noise of the phase (snr) is defined as the maximum signal-to-noise value within 25 s of

242   the phase arrival time; phase arrival times were obtained using an array-based method (Lekić &

243   Fischer, 2014). The second quality factor is the correlation coefficient ($corr$) of the R and Z

244   components in a 3.5 s window around the phase arrival time. The weighting factor is equal to

245   the product of these factors if snr is greater than 5 and $corr$ is greater than 0.95. Otherwise the

246   weighting factor is set to zero and the phase is discarded. After obtaining individual β_0^{FS} values

247   (equations 4 & 6) and their weights from P arrivals, the station free-surface shear velocity β_s^{FS} is

248   defined as the weighted mean of the individual values. Assuming β_s^{FS}, individual α_0^{FS}

249   measurements and their weights are obtained from S arrivals, and the station compressional

250   velocity α_s^{FS} is calculated using a weighted average. If the number of non-zero weighted P

251   arrivals is less than four, β_s^{FS} is set to 2.8 km/s, and if the number of non-zero weighted S

252   arrivals is less than four, α_s^{FS} is set to $1.8\beta_s^{FS}$.

253   To show how the method works well with real data, the free surface velocity determination was

254   applied to data from station ISP (GE network). The free-surface velocities α_s^{FS} and β_s^{FS} for this

255   station are the same as the input velocity model used in the synthetic case in Figure 3. Figures

256   S1a to S1c show the $\mathbf{C_1}$ - $\mathbf{C_3}$ patterns for a P arrival from an earthquake that occurred on 20 July

257   2014 at ~44.65°N, 148.78°E with a ray parameter equal to that of the P arrival in the synthetic

258   case in Figure 3. The observed patterns are very similar to the synthetic patterns, except for $\mathbf{C_3}$

259   (Figure S1c) where the transformed SV component is not as successfully minimized as in the

260   synthetic case. The misfit functions from the grid search result are also similar to those from the

261   synthetic case (Figure 4a versus Figure 3d) with a β_0^{FS} of 2.82 km/s obtained at the minimum

262   misfit. Values of β_0^{FS} were also obtained for P arrivals from other earthquakes, and their

263   histogram is shown in Figure 5a. Although different arrivals resulted in different β_0^{FS} values, their

264   distribution centers around the weighted mean for β_s^{FS} 2.82 km/s nearly symmetrically. The $\mathbf{C_1}$ -

265    $\mathbf{C_3}$ patterns (Figure S1d to S1f) for an S arrival (from an earthquake that occurred on 18 May

266   2014 at ~4.25°N, 92.76°E with a ray parameter equal to that of the S arrival synthetic case in

267   Figure 3) are similar to those from the synthetic case with minor differences. The grid search

268   (Figure 4b) yields misfit functions that are similar to the synthetic case (Figure 3h), with an α_0^{FS}

269   clearly defined at a value of 4.92 km/s. The distribution of α_0^{FS} values from different S arrivals

270   shows greater variability than the β_s^{FS} distribution from the P arrivals (Figure 5b versus Figure

271   5a). This result is partly because the S polarization dependence on α_0^{FS} is weaker than on β_0^{FS}

272   (Park & Ishii, 2018), and the number of P arrivals with non-zero weights is five times of the

273   number of S arrivals with non-zero weights since P phases generally have a higher signal-to-

274   noise ratio. Nonetheless, the α_0^{FS} distribution is still broadly centered around its weighted mean

275   of 4.92 km/s.

276   After obtaining α_s^{FS} and β_s^{FS}, the P and SV components are calculated with equation (1) by

277   setting $\alpha^{FS} = \alpha_s^{FS}$ and $\beta^{FS} = \beta_s^{FS}$. The P and SV components for the P and S arrivals employed

278   in Figure 4 are plotted in Figures 4c and 4d. The SV component is minimal over the P arrival

279   window, and the P component is minimal over the S arrival window, indicating the success of

280   the transform with our new approach to finding free-surface velocities.

281

282   2.2. Kernel Based Common-Conversion Point Stacking

283   To better incorporate converted wave scattering into CCP stacking, we have developed spatial

284   functions that describe how an individual Sp or Ps receiver function contributes to the stack,

285   based on Sp and Ps sensitivity kernels (e.g. Hansen & Schmandt, 2017; Hua et al., 2020;

286   Mancinelli & Fischer, 2017). During CCP stacking of Sp or Ps receiver functions, phase ray

287   paths are traced to a given depth and the travel-time of the converted phase from that point to the

288   station identifies the relevant amplitude from the receiver function. To calculate the stack at a

289   given horizontal location for that depth, receiver function amplitudes are combined, assuming

290   amplitude relationships between the location in the stack and the position of ray paths. In prior

291   studies, these relationships have typically been described as geographic bins (e.g. Dueker &

292   Sheehan, 1997) or with weighting functions based on vertical path Fresnel zones (e.g. Lekić &

293   Fischer, 2017; Lekic et al., 2011; Wittlinger & Farra, 2007). Here we develop weighting

294   functions that more accurately reflect the interaction of Sp and Ps phases with velocity structure

295   using their sensitivity kernels.

296   The time-dependence of scattering can be illustrated by incident and scattered wave ray paths

297   (Figure 6). An incident wave travels upward in the radial-vertical plane (*r-z* plane). The incident

298   wave encounters a scatterer, a scattered wave is generated and propagates upward to the station,

299   and it may not travel in the *r-z* plane. The incident wave travel time from the earthquake location

300   to the station is defined as τ_i^r, and the incident wave travel time from the earthquake to the

301   scatterer is defined as τ_i^s. The travel time of the scattered wave from the scatterer to the station

302   is given as τ_j. The phase delay time between the scattered phase and the incident phase

303   (equivalent to time in the receiver function) is described as

$$T = \tau_i^s + \tau_j - \tau_i^r. \tag{7}$$

305   Scatterers sharing the same T form the phase delay isochron (e.g. Bostock & Rondenay, 1999;

306   Bostock et al., 2001). Energy from scatterers on the same isochron contributes to receiver

307   function amplitude at the same time, and the isochrons determine the shape of the scattering

308   kernels for receiver function amplitudes (e.g. Bostock & Rondenay, 1999; Bostock et al., 2001;

309   Hansen & Schmandt, 2017; Hua et al., 2020; Mancinelli & Fischer, 2017). This formulation is

310   based on the Born approximation that scattered waves will not be scattered again, so the travel

311   time difference can be expressed as equation (7).

312   The shapes of the phase delay isochrons for Sp and Ps phases fundamentally differ. An Sp

313   isochron is illustrated in Figure 7a. This example corresponds to a uniform half space with

314   V_p=7.8 km/s and V_s=4.3 km/s (typical upper mantle values), an incident S wave ray parameter of

315   0.1098 s/km (same as used in Figures 4 & 5), and a 200 km scattering depth (the depth where the

316   converted wave ray path intersects the isochron). For this case, the Sp isochron correponds to a

317   delay time of -27.76 s. The isochron is horizontal near its minimum depth at the conversion

318   point (the intersection point with the converted wave ray path), dips more steeply elsewhere, and

319   extends to infinite distance. A Ps isochron is shown in Figure 7b, for an incident P wave ray

320   parameter of 0.0482 s/km (same as used in Figures 4 & 5) and a scattering depth of 200 km.

321   Here the Ps isochron correponds to a delay time of 21.74 s. The isochron is also horizontal

322   around the conversion point, but this is the maximum depth on the isochron. In addition, the flat

323   portion of the Ps isochron is much smaller than for the Sp isochron, the Ps isochron does not

324   extend to infinite distance, and its slope angle can be as large as 90°.

325   Based on our knowledge of the isochrons, we developed a spatial weighting function for CCP

326   stacking. The weighting function is based on the slope of the isochron, the geometrical distance

327   from the scatterer to the station, and the depth offset between the scattering depth and the

328   isochron. Each of these factors is discussed below.

329   An assumption inherent in CCP stacking is that velocity discontinuities are horizontal over the

330   length scales where amplitudes from different individual converted phases (or receiver functions)

331   are combined. To be consistent with converted phase sensitivity kernels, the amplitude

332   weighting functions that describe these length scales should correspond to the portion of the

333   isochron that is sensitive to horizontal structure, and what controls the sensitivity to discontinuity

334   dip is the slope angle of the isochron (Rondenay et al., 2005). When a discontinuity overlaps

335   with an isochron in space, scatterers on the discontinuity generate scattered waves that are

336   recorded by the station at the same time, and the positive interference of the scattered waves

337   produces a clear phase in the receiver function. Therefore, for CCP stacking, receiver function

338   amplitudes should be projected into the stack along a depth interface only where their isochron

339   slope angle is approximately 0°. This approach differs from migration methods that are designed

340   to image discontinuities with an arbitrary dip angle and in which receiver function amplitude are

341   projected along the whole isochron (e.g. Hua et al., 2020; Zhang & Schmandt, 2019).

342   The isochron slope angle is equal to the angle between the phase delay time gradient (∇T) and

343   the vertical axis, and can be derived in a similar manner to Hua et al. (2020). From the path

344   geometry in Figure 6, it can be seen that

$$\frac{\partial \tau_i^s}{\partial r} = \frac{\sin\theta_i}{v_i}, \quad \frac{\partial \tau_i^s}{\partial t} = 0, \quad \frac{\partial \tau_i^s}{\partial z} = -\frac{\cos\theta_i}{v_i},$$

345   (8)

$$\frac{\partial \tau_j}{\partial r} = -\frac{\sin\varphi}{v_j}, \quad \frac{\partial \tau_j}{\partial t} = \frac{\sin\phi}{v_j}, \quad \frac{\partial \tau_j}{\partial z} = \frac{\cos\theta_j}{v_j},$$

346   where v_i is the incident wave velocity, v_j is the scattered wave velocity, θ_i is the angle from

347   vertical of the incident wave path, θ_j is the scattered wave take-off angle, φ and ϕ are two

348   angles defined in Figure 6. φ is positive when the scattered wave is traveling in the positive r

349   direction, and ϕ is positive when the scattered wave is traveling in the negative t direction.

350   Because τ_i^r does not depend on the scatterer location, from equations (7) and (8), the gradient of

351   T is expressed as

$$\nabla T = \left(\frac{\sin\theta_i}{v_i} - \frac{\sin\varphi}{v_j}\right)\mathbf{e}_r + \frac{\sin\phi}{v_j}\mathbf{e}_t + \left(\frac{\cos\theta_j}{v_j} - \frac{\cos\theta_i}{v_i}\right)\mathbf{e}_z$$

352   (9)

353   where $\mathbf{e}_r$, $\mathbf{e}_t$ and $\mathbf{e}_z$ are unit vector in r, t and z directions. From equation (9), and with some

354   algebra, the slope angle ϑ is expressed as

$$\vartheta = \arctan\left(\frac{\sqrt{v_i^2 \sin^2 \phi + \left(v_j \sin\theta_i - v_i \sin\varphi\right)^2}}{v_j \cos\theta_i - v_i \cos\theta_j}\right). \tag{10}$$

356   To simplify, φ and ϕ are replaced by the dihedral angle between the vertical plane of scattered

357   wave propagation and the r-z plane (γ) through the geometric relationship

$$\sin\phi = \sin\theta_j \sin\gamma, \quad \sin\varphi = \sin\theta_j \cos\gamma, \tag{11}$$

359   where γ is positive when the scattered wave is traveling the positive r direction. By substituting

360   equation (11) into (10), the slope angle is expressed as

$$\vartheta = \arctan\left(\frac{\sqrt{v_i^2 \sin^2\theta_j + v_j^2 \sin^2\theta_i - 2v_i v_j \cos\gamma \sin\theta_i \sin\theta_j}}{v_j \cos\theta_i - v_i \cos\theta_j}\right). \tag{12}$$

362   To obtain ϑ, v_i and v_j are taken from an existing velocity model, and γ is calculated as the

363   difference between the earthquake back-azimuth and the azimuth from the station to the

364   scatterer. Because teleseismic events are used, p, the ray parameter, is assumed to be invariant

365   with horizontal location. Based on Snell's law, the incident wave vertical incidence angle is

366   expressed as

$$\theta_i = \arcsin\left(\frac{v_i R_E p}{R_E - z}\right) \tag{13}$$

368   where R_E represents the earth radius, and z is the depth of the scatterer. To obtain θ_j, at each

369   station, the 1D velocity structure traversed by the scattered phase is extracted from an existing

370   velocity model, and 1000 rays whose ray parameters range from 0 s/km to the maximum value

371   (i.e. the ray parameter for a horizontal wave at the surface) with a uniform increment are shot

372   from the station. All points along each of the 1000 paths are labeled with their corresponding ray

373   parameter, and scattered wave ray parameters for all locations in space can then be retrieved by

374   interpolating the ray parameter relationship. θ_j is obtained by substituting the scattered wave ray

375   parameter and v_j into equation (13).

376   To help visualize isochron slope angles, slope angle values from equation (12) are color-coded

377   on the isochrons in Figure 7. The near-horizontal region is much larger on the Sp isochron than

378   on the Ps case, even though the isochrons are sampling a horizontal discontinuity at the same

379   depth. In contrast, the Ps isochrons have larger regions with steeper dips including significant

380   near-vertical portions, explaining the ability of Ps receiver functions to image vertical

381   discontinuities (e.g. Hansen & Schmandt, 2017). The slope angle distribution of points at 200 km

382   depth for the Sp case in Figure 7a is shown in Figure 8a. The slope angle is minimized around

383   the conversion point in a zone that is elongated in the r direction and symmetric about the r axis.

384   While isochrons control the overall shape of the scattering kernel, their overall amplitude is

385   scaled by geometric spreading of the scattered wave from the scatterer to the station, and

386   geometric spreading is to the first order inversely proportional to the geometric distance from the

387   station to the scatterer (Hansen & Schmandt, 2017). Geometric distance from points at 200 km

388   depth for the case in Figure 7 is shown in Figure 8b, where the smallest values lie below the

389   station. During CCP stacking of Sp phases, although some points far from the station may have a

390   relatively flat isochron, the receiver function amplitude should not make a significant

391   contribution there because of the small geometric spreading value.

392   A third consideration is that receiver function amplitudes for a given converted wave ray path

393   should not be projected to locations in the CCP stack where the depth offset between the

394   isochron and the conversion point (e.g. the offset between the isochron and 200 km depth in

395   Figure 7) is large. To estimate the depth offset at different locations, the slope angles of the

396   isochron along the r axis (ϑ_r) and t axis (ϑ_t) are calculated based on the direction of ∇T in

397   equation (9), and are expressed as

398
$$\vartheta_r = \arctan\left(\frac{v_i \sin\theta_j \cos\gamma - v_j \sin\theta_i}{v_j \cos\theta_i - v_i \cos\theta_j}\right), \quad \vartheta_t = \arctan\left(-\frac{v_i \sin\theta_j \sin\gamma}{v_j \cos\theta_i - v_i \cos\theta_j}\right). \tag{14}$$

399   The depth offset (Δz) is then estimated to the first order as

400
$$\Delta z = \tan \vartheta_r \Delta r + \tan \vartheta_t \Delta t \qquad (15)$$

401   where Δr and Δt are the horizontal offsets from the imaging location to the conversion point in

402   the r and t directions. For the case in Figure 7a, the true depth offset that is directly measured by

403   calculating the depth difference between the isochron and 200 km depth is shown in Figure 8c,

404   and the Δz estimate based on equation (15) is shown in Figure 8d. The first order values from

405   equation (15) reflect the true depth offset reasonably well closer to the conversion point, but at

406   more distant locations, equation (15) tends to overestimate the depth offset. However, because

407   receiver function amplitudes should be projected to locations where the depth offset is small,

408   such overestimation helps to make our stacking method more conservative.

409   A weighting function, W_1, was designed to limit the projection of receiver function amplitudes to

410   stack locations with relatively flat isochrons, smaller distances to the station and smaller depth

411   offset to the isochron.

412
$$W_1 = \frac{z}{d} \exp\left(-\frac{\vartheta^2}{2\sigma_\vartheta^2}\right) \exp\left(-\frac{\Delta z^2}{2\sigma_z^2}\right), \qquad (16)$$

413   where z is the depth of the imaging point in the stack, and d is the geometrical distance from

414   the station to the imaging point. σ_ϑ is a slope angle threshold, and at points with ϑ larger than

415   σ_ϑ amplitudes are down-weighted. σ_z depth offset threshold, with a similar function relative to

416   Δz. In practice σ_ϑ is chosen to be 5°, and σ_z is calculated by

417
$$\sigma_z = T_{RF} \frac{dz}{dT_j}, \qquad (17)$$

418   where T_{RF} is the half-width of the Gaussian that is convolved with the receiver function during

419   time-domain deconvolution (Ligorria & Ammon, 1999) to smooth the receiver function. T_j is

420   the phase delay time (defined in the same way as T) along the converted wave ray path, while

421   dz/dT_j is the inverse of its vertical derivative. Therefore, σ_z characterizes the vertical imaging

422   uncertainty that is introduced during receiver function generation.

423   Weighting functions are distorted ellipses that have their maxima at the conversion point and are

424   elongated in the r direction. The Sp weighting function for the case in Figure 7a is illustrated in

425   Figure 8e, while the weighting function for the Ps example is shown in Figure 8f. For mantle

426   discontinuities at the same depth, the Ps weighting function occupies a much smaller area,

427   indicating that CCP stacking without artificial interpolation or smoothing requires denser station

428   spacing for Ps phases than for Sp. Because of the broader lateral extent of their weighting

429   functions, CCP stacking of Sp phases is better suited to imaging near-horizontal discontinuities

430   with stations spaced at more than 20-30 km. In addition, CCP stacking of Sp phases avoids

431   artifacts related to crustal reverberations that are often strong features in Ps CCP images.

432   To calculate the CCP stack in practice, W_1 is set to zero where its value is less than 0.02 or the

433   horizontal angular distance to the station is more than 10°. To weight all receiver functions

434   equally, a normalized weighting function, W_2, is calculated as:

435
$$W_2 = \frac{W_1}{\sum_{horizontal} W_1}. \tag{18}$$

436   W_2 is simply W_1 divided by the sum of all W_1 at the same depth, so it would add up to one at

437   each depth, and thus different receiver functions are weighted identically. At each imaging point,

438   the CCP stacked receiver function amplitude (RF_s) can be expressed as

439
$$RF_s = \frac{\sum_k (W_2)_k RF_k}{\sum_k (W_2)_k}, \tag{19}$$

440   which is the weighted average of individual receiver function amplitudes (RF_k) from different

441   records, and the subscript k refers to the index of the individual record.

442

443   2.3. The Standard Deviation of a Weighted Average

444   In order to interpret a CCP stack, knowledge of the uncertainties in the stack amplitude are

445   necessary to assess which structural features have amplitudes that exceed the uncertainty

446   threshold.   In some previous studies, the stack amplitude uncertainty was estimated by

447   bootstrapping the CCP stacking process (e.g. Hua et al., 2018). The CCP stack was constructed

448   multiple times based on random samples of the receiver functions, and these individual stacks

449   were represented by their bootstrap mean at each point, with the bootstrap standard deviation at

450   each point indicating the uncertainty. However, receiver functions often number in the tens of

451   thousands, with thousands of receiver functions contributing to each image point. This volume

452   of data requires a very large number of CCP stack iterations to get a reliable standard deviation

453   from bootstrapping, resulting in a high computational cost. Therefore, we have developed a new

454   approach to measuring the standard deviation of a weighted average. In particular, this approach

455   is appropriate for cases where the sums of the weights are allowed to vary while the weights

456   themselves could be dependent on the sample.

457   For a weighted average in the same form as equation (19), when the number of samples (n) is

458   large enough, the central limit theorem indicates that the weighted average of a random sample

459   can be expressed as

$$\frac{\sum wx}{\sum w} = \frac{\frac{1}{n}\sum wx}{\frac{1}{n}\sum w} \cong \frac{\mu_{wx} + \frac{1}{\sqrt{n}}\sigma_{wx}\varepsilon_1}{\mu_w + \frac{1}{\sqrt{n}}\sigma_w\varepsilon_2}, \tag{20}$$

461   where w is the weight and x is the sample value, μ_{wx} and μ_w stand for expected values of wx

462   and w, σ_{wx} and σ_w are standard deviations for wx and w, and both ε_1 and ε_2 follow the

463   normal distribution $N(0,1)$. For equation (20) to be valid, samples are required to be

464   independent and with the same distribution, and the same is true for the weights. However, the

465   weights do not necessarily need to be independent of the samples. When n is large enough,

466   equation (20) can be approximated by a Taylor expansion as

467

$$\frac{\mu_{wx} + \frac{1}{\sqrt{n}}\sigma_{wx}\varepsilon_1}{\mu_w + \frac{1}{\sqrt{n}}\sigma_w\varepsilon_2} = \frac{1}{\mu_w}\left(\mu_{wx} + \frac{1}{\sqrt{n}}\sigma_{wx}\varepsilon_1\right)\left[1 - \frac{1}{\sqrt{n}\mu_w}\sigma_w\varepsilon_2 + O\left(\frac{1}{n}\right)\right],$$

$$= \frac{1}{\mu_w}\left[\mu_{wx} - \frac{\mu_{wx}}{\sqrt{n}\mu_w}\sigma_w\varepsilon_2 + \frac{1}{\sqrt{n}}\sigma_{wx}\varepsilon_1 + O\left(\frac{1}{n}\right)\right]$$

(21)

468   The first term in the bracket characterizes the expectation of the average, while the other two

469   terms characterize the variability of the weighted average. Therefore, the expectation (E) and

470   the variance (V) of the weighted average are expressed as

471

$$E\left(\frac{\sum wx}{\sum w}\right) = \frac{\mu_{wx}}{\mu_w}$$

$$V\left(\frac{\sum wx}{\sum w}\right) = \frac{1}{n\mu_w^2}V\left(\sigma_{wx}\varepsilon_1 - \frac{\mu_{wx}}{\mu_w}\sigma_w\varepsilon_2\right)$$

$$= \frac{1}{n\mu_w^2}\left[\sigma_{wx}^2 + \frac{\mu_{wx}^2}{\mu_w^2}\sigma_w^2 - \frac{2\mu_{wx}}{\mu_w}\sigma_{wx}\sigma_w Corr(\varepsilon_1, \varepsilon_2)\right]$$

(22)

472   and the correlation $Corr$ can be expressed as

473

$$Corr(\varepsilon_1, \varepsilon_2) = Corr\left(\sum wx, \sum w\right) = \frac{Cov\left(\sum wx, \sum w\right)}{\sqrt{V\left(\sum wx\right)V\left(\sum w\right)}}$$

(23)

474   based on the central limit theorem (equation 20), where Cov stands for covariance. The sample

475   covariance $Cov\left(\sum wx, \sum w\right)$ is equal to n times the population covariance $Cov(wx, w)$, since

476   Cov is a bilinear operator and samples are independent. The correlation in equation (23) can be

477   further derived as

478

$$Corr(\varepsilon_1, \varepsilon_2) = \frac{nCov(wx, w)}{\sqrt{n^2 V(wx)V(w)}} = \frac{Cov(wx, w)}{\sigma_{wx}\sigma_w},$$

(24)

479   In practice, μ_{wx}, μ_w, σ_{wx}, σ_w and $Cov(wx, w)$ can be estimated from samples as

480 $$\mu_{wx} = \overline{wx}, \quad \mu_w = \overline{w}, \quad \sigma_{wx} = \sqrt{\overline{w^2 x^2} - \left(\overline{wx}\right)^2}, \quad \sigma_w = \sqrt{\overline{w^2} - \left(\overline{w}\right)^2}, \quad Cov(wx, w) = \overline{w^2 x} - \overline{wx}\,\overline{w},$$

481 (25)

482 where the bar indicates the sample average. By substituting equations (24) and (25) into equation

483 (22), and after some algebra, the standard deviation (Std) of the weighted average, which is the

484 square root of the variance in equation (22), can be expressed as

485 $$Std\left(\frac{\sum wx}{\sum w}\right) = \frac{\sqrt{\left(\sum w^2 x^2\right)\left(\sum w\right)^2 + \left(\sum w^2\right)\left(\sum wx\right)^2 - 2\left(\sum w\right)\left(\sum wx\right)\left(\sum w^2 x\right)}}{\left(\sum w\right)^2}, \quad (26)$$

486 In the case of CCP stacking, where x is receiver function amplitude and w is W_2, equation (26)

487 characterizes the uncertainty of stack amplitude at each point in the stack volume. However, this

488 expression can also be applied to any weighted mean where samples are independent but drawn

489 from the same distribution, and weights are independent but drawn from the same distribution.

490 To show the effectiveness of the standard deviation expression in equation (26), a numerical

491 experiment was designed. We randomly generated 648 samples based on a normal distribution

492 $N(0.02, 0.08^2)$, and the corresponding weights were randomly generated based on a normal

493 distribution $N(0.7, 0.4^2)$. The histograms of the resulting samples and weights are shown in

494 Figures 9a and 9b, and the standard deviation of the weighted mean of these data from equation

495 (26) is shown by the black line in Figure 9c. For comparison, 50,000 iterations of bootstrapping

496 were also performed on these data. In each iteration, 648 random values were drawn from the

497 samples and weights, and their weighted average was calculated. After each iteration, the

498 estimated standard deviation of the weighted averages based on the last and all previous

499 iterations was calculated. For this case, the bootstrapped standard deviation starts to converge to

500 a stable value after ~1,000 iterations, and the value it converges to is very close to the weighted

501 standard deviation from equation (26) which is based on only one calculation. To show how

502 these standard deviation estimates compare to the true standard deviation, a Monte Carlo

503 simulation was designed. Instead of using one set of sample and weights (Figures 9a & 9b) as in

504 the bootstrap case, at every iteration, a new set of sample and weights was generated based on

505 the true distribution, and the weighted average was calculated. Then, the standard deviation

506   calculated from the last on all previous sets of sample and weights was stored. The weighted

507   standard deviation from the Monte Carlo simulation converges to a value which should

508   approximate the true standard deviation (Figure 9c). This value is close to the equation (26)

509   weighted standard deviation, but is offset by a small amount, because the single set of samples

510   and weights used in equation (26) does not strictly follow the overall distributions. However, the

511   good agreement between the estimate from equation (26) and both the true and bootstrap

512   standard deviations demonstrates the accuracy of the much more efficient equation (26)

513   approach.

514   We also compared the weighted standard deviation from equation (26) to the bootstrap standard

515   deviation from the receiver function data in the real CCP stack (Figure 9d). In this example, for

516   an imaging point located at 40.5°N, 38°E and 125 km depth, there are 648 individual receiver

517   functions that have non-zero W_2 (equation 18). However, because in practice bootstrapping of

518   the CCP stack would be performed over all 23,787 receiver functions, the sample size in this

519   example is 23,787, although only 648 samples have non-zero weights. Again the weighted

520   standard deviation from equation (26) equals the value to which the bootstrapping converges,

521   although in this case reasonable convergence requires ~600 iterations.

522   Therefore, the approach summarized in equation (26) is an accurate and computationally fast

523   means of calculating the standard deviation of a weighted average, and is applicable to CCP

524   stacking, but also to a wider range of problems. This approach is especially suitable for

525   problems where the sum of the weights is not fixed, since a much simpler expression can be used

526   when the sum is fixed. For example, equation (26) can also be used to quantify the standard

527   deviation of the measured free-surface velocity in Section 2.1. In addition, equation (26) is also

528   powerful in the sense that it does not require the weight to be independent of the sample value,

529   since the correlation between the weighted sum and the sum of the weights (equation 24) is

530   considered in the derivation.

531

532   **3. Data Processing and CCP Stacking**

533   Data used in this study are Sp phases from broadband seismograms recorded from as early as

534   1990 to 2019 by 453 seismic stations around the Anatolian region (Figure 1) available from the

535   International Federation of Digital Seismograph Networks (FDSN). Among all the stations, 153

536   of them are permanent stations from the network KO (Kandilli Observatory and Earthquake

537   Research Institute Bosphorus Univ., 2001). Other contributing stations consist of 58 permanent

538   stations from 10 networks (GE, HL, TU, CQ, HT, GO, HC, MN, IU, AB) and 242 temporary

539   stations from 14 networks (YB, YL, YI, XW, XY, Z3, ZZ, XO, XH, YF, TK, SU, SD). Network

540   references appear in the Acknowledgements.

541   Seismic records were retrieved for earthquakes with epicentral distances between 30° and 90°

542   and a minimum moment magnitude of 5.8. To determine appropriate phase windows for P and S

543   arrivals, the arrival time of the phases was picked using an array-based method (Lekić & Fischer,

544   2014) that results in more robust phase identification than from individual records. The

545   seismograms were then filtered by a 4-100 s bandpass filter, and the free-surface velocities are

546   calculated based on the method described in section 2.1. In addition, 2-20 s and 10-100 s

547   bandpass filters were also used to help better detect different velocity structures, and will be

548   discussed in section 4. After retrieving the free-surface velocities, the P and SV components of

549   the seismic records were calculated from equation (1). The signal-to-noise ratios of the S phases

550   were then measured from the SV component, using the ratio of the mean amplitude in a 5 s

551   signal window to the mean amplitude in a 25 s noise window.

552   Sp receiver functions were then obtained by deconvolving the SV component of the direct S

553   arrival from the P component which contains the Sp precursors. Deconvolution was performed

554   using a time-domain deconvolution method (Ligorria & Ammon, 1999).   The resulting impulse

555   responses were convolved with a Gaussian whose half-width is 1 s and whose peak value is 1.

556   However, while P and S phases from all distances were used for measuring the free-surface

557   velocity, only earthquakes with epicentral distances between 55° and 85° were used to generate

558   Sp receiver functions. We then eliminated receiver functions with a signal-to-noise ratios of less

559   than two, or for which the difference between the arrival time determined from the array-based

560   method and the prediction of the AK135 reference model (Kennett et al., 1995) is more than 10

561   s. With these criteria, 66,693 Sp receiver functions were generated.

562   To migrate the receiver functions to depth, we used 1D velocity models that reflect velocity

563   along the converted P phase ray path from the recent full-waveform inversion model (Blom et

564   al., 2020). Using a model derived from full-waveform inversion is advantageous because

565   absolute velocities are inverted for directly, and because this method is especially well suited for

566   areas with significant heterogeneity such as Anatolia. For stations outside the limits of the

567   velocity model, the velocity at the closest location was used. Instead of directly using V_p from

568   Blom et al. (2020), we calculated the average V_p / V_s at every depth in the study region (33°-

569   45°N and 23°-48°E) and used the average V_p / V_s multiplied by V_s to obtain V_p. V_s is better-

570   resolved than V_p in the model of Blom et al. (2020) for two reasons. First, because V_s is always

571   lower than V_p, sensitivity kernels for this parameter are more spatially constrained than those for

572   V_p and thus contain more detail. Second, full-waveform inversion models are dominated by

573   surface waves, which naturally have stronger sensitivity to V_s. Our approach avoids zones with

574   unrealistic V_p/V_s values due to this heterogeneous sensitivity. The V_s model used in this paper

575   for migration is the shear velocity model corresponding to SV particle motion.

576   A range of criteria were applied to the migrated receiver functions to eliminate outliers. A

577   prominent Moho is evident across the study region both in this study and in prior work (e.g.

578   Abgarmi et al., 2017; Frederiksen et al., 2015; Karabulut et al., 2019; Licciardi et al., 2018;

579   Ozacar et al., 2008; Vanacore et al., 2013; L. Zhu et al., 2006; Zor et al., 2003). Since the Moho

580   predicts strong negative phases in Sp receiver functions, we discarded receiver functions without

581   such signals at shallow depths. Receiver function negative amplitudes in the range from 15 km to

582   60 km depth were used to form a vector $\mathbf{rf}_{sn}$, and receiver functions with $\left\|\mathbf{rf}_{sn}\right\|_2^2$ smaller than

583   20% of the median $\left\|\mathbf{rf}_{sn}\right\|_2^2$ from all receiver functions were discarded. In addition, using positive

584   amplitudes between 15 km and 60 km depth to form the vector $\mathbf{rf}_{sp}$, receiver functions with

585    $\left\|\mathbf{rf}_{sp}\right\|_2^2$ greater than 3 times the median $\left\|\mathbf{rf}_{sp}\right\|_2^2$ from all receiver functions were discarded. With

586   these two Moho related quality control criteria, receiver functions without obvious Moho phases

587   are removed (second and third columns in Figure S2).

588   Other criteria remove receiver functions with large and physically non-plausible amplitude

589   variations. Receiver function amplitudes predicted by the Blom et al. (2020) model provide a

590   reasonable benchmark for plausible receiver function amplitudes.   For the minimum, median

591   and maximum S wave ray parameters of all seismic records, synthetic seismograms were

592   calculated for Vs as a function of depth from Blom et al. (2020) at 1˚ horizontal increments,

593   using the propagator matrix method (Keith & Crampin, 1977). Receiver functions were

594   generated from the synthetic waveforms using the same approach that was applied to the data.

595   From the synthetic receiver functions for the entire study region, the minimum ($\mathbf{rf}_{min}$) and

596   maximum ($\mathbf{rf}_{max}$) amplitudes were found, together with their mean value ($\mathbf{rf}_{mean}$). The half-

597   width of the amplitude range $\mathbf{rf}_{hw}$ was defined as $(\mathbf{rf}_{max} - \mathbf{rf}_{min})/2$. To eliminate observed

598   receiver functions ($\mathbf{rf}$) with abnormally large amplitudes, receiver functions with $\left\| \mathbf{rf} - \mathbf{rf}_{mean} \right\|_2^2$

599   greater than five times the median $\left\| \mathbf{rf} - \mathbf{rf}_{mean} \right\|_2^2$ from all receiver functions were discarded. This

600   criterion only discards receiver functions that have enormously large amplitudes, and the number

601   of receiver function removed by this step is relatively small (fourth column in Figure S2).

602   However, it is a useful tool to eliminate obviously unrealistic receiver functions, for example

603   cases with a single huge peak near zero time that typically reflect bad data. In addition, to

604   remove sustained large amplitudes in the mantle which are completely inconsistent with Blom et

605   al. (2020) model, depth layers greater than 60 km where the receiver function amplitude $\mathbf{rf}$ is

606   either smaller than $\mathbf{rf}_{mean} - 0.8\mathbf{rf}_{hw}$ or larger than $\mathbf{rf}_{mean} + 0.8\mathbf{rf}_{hw}$ were counted, with their number

607   indicated as n_d . We then discarded all receiver functions with n_d larger than the median of n_d

608   from all receiver functions. The n_d criterion is the strictest test we applied, as it removes half of

609   the data, and it significantly reduces noise in the mantle depth range (fifth column in Figure S2).

610   With these four quality control criteria, unrealistic receiver functions are effectively removed

611   (sixth column versus first column in Figure S2). However, the same primary phases appear in

612   the stack in all cases, and the only significant change is that adding any one of the other criteria

613   (columns two to four in Figure S2) to the initial signal-to-noise threshold (column one in Figure

614   S2) increases the amplitude of the phase at depths of 100-150 km in this location.

615   CCP stacking was applied to the remaining 23,787 receiver functions (as described in Section

616   2.2), and the stack uncertainties were calculated (Section 2.3). The conversion points at 125 km

617   depth (Figure 10) illustrate that much of the Anatolian region is sampled by the measurements.

618   At each node in a grid with 0.1˚ spacing horizontally and 0.5 km spacing in depth, the migrated

619   receiver functions were stacked based on equation (19), and the standard deviation of the stacked

620   result was estimated by equation (26). To quantify the amount of receiver function information at

621   each point in the stack, the weights for individual receiver functions at the same node were

622   summed $\sum W_2$ (equation 18) to obtain a value called W_s. Only features with relatively large W_s

623   were interpreted, partly to ensure sufficient data were used for the stacking at the place, and

624   partly because the standard deviation formulation (equation 26) is only valid when the number of

625   samples is large enough. However, because receiver functions were not projected to depths

626   where the ray parameter is larger than the critical ray parameter of the P wave, the horizontal

627   sum of W_s at greater depths is always smaller than the sum at smaller depths. Therefore, in order

628   to eliminate bias due to this effect, W_s is normalized to a new depth-insensitive weighting W_3 as

629
$$W_3 = \frac{W_s}{\sum\limits_{horizontal} W_s} \cdot \frac{\left(\sum\limits_{vertical} \sum\limits_{horizontal} W_s \right)}{n_{layer}}, \qquad (27)$$

630   where n_{layer} is the number of depth layers (901 in this study). CCP stacking results were only

631   interpreted at points with W_3 over 0.4. The W_3 distribution of the region at 125 km depth is

632   shown in Figure 10, and for most of the continental Anatolian region W_3 exceeds the 0.4

633   threshold for interpretation. In addition, the CCP stack is interpreted only if the standard

634   deviation is less than 0.01 or less than half of the weighted and stacked receiver function

635   amplitude.

636   As an example, the CCP stack on profile A-A', which crosses the Anatolian region from east to

637   west (Figure 11a), indicates a Moho that is partially imaged (red phase at 30-50 km depth), a

638   410-discontinuity that extends across most of the profile, and a negative velocity gradient at

639   depths of 360-370 km that has been observed elsewhere and interpreted as the top of a low

640   velocity layer just above the 410-discontinuity (e.g. Vinnik & Farra, 2002). We also observe a

641   prominent mantle arrival at depths of 80-150 km, indicative of a velocity increase with depth,

642   that will be discussed further below. A weak positive velocity gradient is also observed around

643   250 – 300 km depth in some locations. Figure 11b shows that the standard deviation of the

644   profile is typically small and uniform below 100 km depth. However, the standard deviation

645   above 50 km is much larger, even at points with large W_3 (Figure 11c), and cannot be interpreted

646   except at points where the Moho Sp phase has a large enough amplitude to exceed twice of the

647   large standard deviation. Unlike the standard deviation, the W_3 weight distribution is highest

648   along groups of dense converted P ray paths and is larger overall above 300 km depth (Figure

649   11c). Because most of the events are from the northeast to east (Figure 10b), deep structures

650   beneath the west end of the profile are not well imaged and are not shown due to small weight

651   values (Figure 11a).

652

4. Results and Discussion

654   To show how the kernel based CCP stacking method introduced in section 2.2, the free-surface

655   velocity determination method introduced in section 2.1, and the chosen velocity model

656   influence the CCP stacking results, we calculated the CCP stack for three additional cases. In the

657   first, we used the same collection of receiver functions, but with the stacking method in Hua et

658   al. (2018), which employed an empirical weighting function defined by a vertical ray Fresnel

659   zone similar to that in Lekić and Fischer (2017) assuming a dominant frequency of 13 s. The

660   result for cross-section A-A' appears in Figure 12a, but because the weighting function here is

661   defined differently from the weighting function in section 2.1, the image is shown where W_3 is

662   more than 40 instead of 0.4. While the same major phases (Moho, 410 discontinuity, negative

663   amplitudes at 80-150 km) appear in both cases, in the kernel based CCP stacking (Figure 11a)

664   they are more continuous, and the rest of the image contains less small-scale variation in

665   amplitude. This improvement is likely the result of the more physically correct weighting

666   function in the kernel-based stack that individually determines the sensitivity to horizontal

667   discontinuities for each individual receiver function and enables them to more correctly interfere

668   at the appropriate location.

669   We also tested the improvement in the clarity of the CCP stack from the new approach to

670   determining free-surface velocities. In this case (Figure 12b) we use the same set of receiver

671   functions and the older stacking method used in Figure 12a, but with the free surface velocity

672   determination method used in Hopper et al. (2014) which is essentially that of Abt et al. (2010).

673   The differences between the two cases are subtle, but the more accurately determined free

674   surface velocities use in Figure 12a result in slightly different amplitudes for the negative phase

675   at 80-150 km depth. This comparison suggests that the new approach provides only an

676   incremental improvement.   Nonetheless, more accurately constrained free surface velocities

677   contribute confidence to the CCP stack, and in addition they are a valuable tool for studying near

678   surface structures (e.g. Park & Ishii, 2018; Park et al., 2019). In addition, this test also indicates

679   that even if free-surface velocities are not estimated very precisely, their influence on mantle

680   CCP stacking is likely not large as long as the values are reasonably accurate.

681   To verify that the velocity model we chose (Blom et al., 2020) to migrate the receiver functions

682   and calculate the CCP stack does not overly influence the CCP stack results, we also employed

683   the kernel based CCP stacking with the velocity model for Anatolia from Fichtner et al. (2013).

684   However, in this case we directly used both V_p and V_s given by the model. The results of this

685   case (Figure 12c) are similar to those obtained when using Blom et al. (2020) (Figure 11a).

686   Noticeable differences are that the negative phase at 80 – 150 km depth is slightly stronger at

687   ~36°E when using Fichtner et al. (2013), but more continuous at 38°E-39°E with Blom et al.

688   (2020), and the 410 discontinuity is in general more continuous with Blom et al. (2020), while a

689   shallower 410 discontinuity is evident at 33-39 °E when using Fichtner et al. (2013).   However,

690   these differences are relatively minor, and the overall agreement indicates that the CCP stack

691   structures are not dramatically influenced by the assumed velocity model.

692   To further explore how data quality criteria influence the CCP stack, we performed the kernel

693   based CCP stacking with the quality control criteria that remove receiver functions with absent

694   Moho phases (Section 3), as well as the signal-to-noise threshold of 2. The Moho criteria relate

695   only to receiver function amplitudes above 60 km depth, so mantle phases do not influence the

696   quality measure. After applying these criteria, 45,872 receiver functions were retained for

697   stacking. This stack contains nearly twice the number of receiver functions used in the final

698   stack, and the individual receiver functions exhibit greater scatter (second and third columns

699   versus the sixth column in Figure S2). Nonetheless, this stack (Figure S3) contains phases

700   similar to those in the final stack (Figure 11a). One difference is that the negative phases at 80-

701   150 km depth are more coherent with stricter quality criteria (Figure 11a) than in the case with

702   only the Moho criteria (Figure S3). This difference is particular noticeable at 38°E-39°E,

703   although it is reversed at 41°E-43°E. Because the receiver functions removed by the stricter

704   criteria contain physically unrealistic energy, we focus our interpretation on the final stack.

705   The negative Sp phase at depths of 80 – 150 km persists widely beneath Anatolia, regardless of

706   the stacking method and migration velocity model. Unlike the Moho and 410 discontinuity,

707   which are expected globally, the negative upper mantle discontinuity is a more unusual feature.

708   This negative Sp phase, which corresponds to a shear velocity increase with depth, is broadly

709   consistent with V_s gradients in the model of Blom et al. (2020). The depth of the Sp phase

710   (Figure 11a) lies near the base of a layer that is dominated by low velocities in the Blom et al.

711   (2019) model (Figure 13a). The calculated vertical V_s gradients Blom et al. (2020) (Figure 13b)

712   agree with the overall position of the negative Sp phase at longitudes of 31°E to 41°E, and from

713   41°E to 44°E, where the CCP stack only shows only weak negative Sp energy that is distributed

714   over a broad range of depths (Figure 11a), vertically-localized positive velocity gradients are also

715   not clearly observed in the velocity model (Figure 13b). However, some features disagree. For

716   example, the positive velocity gradient at 200 km depth from 30°E to 32°E in the Blom et al.

717   (2020) model is not matched clearly by a feature in the CCP stack. Comparison of the CCP stack

718   with V_s and the vertical V_s gradient from Fichtner et al. (2013) (Figures S4a and S4b) show a

719   similar level of agreement. All shear velocity profiles from full-waveform tomography models in

720   this study (Figures 13, S4 & S5) correspond to SV velocity.

721   The widespread presence of the negative Sp phase at depths of 80 – 150 km is demonstrated by

722   other cross-sections through the CCP stack. Cross-section B-B' (Figure 14a) which is south of

723   A-A' also contains the negative Sp phase at 80 – 150 km depth from 29°E to 40°E, as well as

724   from 42°E to 44°E beneath eastern Anatolia. The phase is also observed in north-south striking

725   cross-sections (Figure 15), and it extends from 38°N to 40.5°N in the west (Figure 15a), from at

726   least 37°N to 41°N in central-eastern Anatolia (Figure 15b), and from 37.5°N to 41.5°N in part

727   of easternmost Anatolia (Figure 15c). However, the phase is not strong ubiquitously. Its

728   amplitude and continuity are strongly diminished in much of the region north of 41°N-41.5°N, as

729   shown in Figures 15a and 15b, and in the east-west cross-section C-C' (Figure 14c). This

730   decrease in the amplitude of the negative Sp phase north of the plate boundary broadly correlates

731   with a reduction of the intensity of the low velocity layer whose base it marks, as shown by a

732   comparison of the Blom et al. (2019) shear velocity model on profiles B-B' (Figure S5a) and A-

733   A' (Figure 13) versus C-C' (Figure S5b). A similar trend appears in the shear velocity models of

734   Fichtner et al. (2013), and a third full-waveform inversion that spans Anatolia (H. Zhu, 2018).

735   Lack of Sp data in the northeast corner of the study region limit our ability to assess the

736   northward limit of negative phase amplitudes as far east as 44°E (Figure 15c). However, some

737   waveform inversion models indicate that very low velocity asthenosphere extends further north

738   at longitudes east of approximately 42°E-43°E, relative to the rest of the study region (Blom et

739   al., 2020; H. Zhu, 2018).

740   The spatial distribution of the negative Sp phase, which appears to mark the base of the

741   asthenospheric low velocity zone, differs from the results of prior Sp studies in the region.   The

742   Sp receiver function study by Kind et al. (2015) showed evidence for positive velocity gradients

743   in shallow upper mantle, but the depths where this energy was observed do not always match our

744   results. In Angus et al. (2006), positive velocity gradients were not observed from Sp phases in

745   the 90-150 km depth range. However, much of the region sampled in Angus et al. (2006) lies in

746   eastern Anatolia where the Sp CCP stack presented here shows only a weak positive Sp arrival

747   (e.g. 40°E to 43°E in Figures 11a & 14a), indicating that this study and our results are not

748   incompatible.

749   The anomalously low velocity asthenosphere beneath Anatolia, whose lower margin is indicated

750   by the negative Sp phase, is observed by many seismic studies. In addition to the full-waveform

751   inversion studies described above (Blom et al., 2020; Fichtner et al., 2013; H. Zhu, 2018), low

752   velocity asthenosphere is also observed beneath the Anatolian region by surface wave

753   tomography (Bakırcı et al., 2012; Salaün et al., 2012) and P wave tomography (Portner et al.,

754   2018; Wei et al., 2019). Prior studies also found low Pn wave velocity (Gans et al., 2009; Mutlu

755   & Karabulut, 2011) and high Sn wave attenuation (Gök et al., 2003) beneath a large portion of

756   Anatolia. All of these studies are consistent with anomalously high mantle temperatures, which

757   have also been indicated by multiple geochemical studies (McNab et al., 2018; Nikogosian et al.,

758   2018; Reid et al., 2017). In addition, elevated mantle V_p/V_s ratios (H. Zhu, 2018) as well as the

759   presence of young magmatism (<10 Ma) across the study region (McNab et al., 2018;

760   Nikogosian et al., 2018; Reid et al., 2017) indicate that low velocities in the asthenospheric layer

761   could be enhanced by the presence of partial melt, leading to unusually strong negative Sp

762   energy from the base of this layer. Other regions with a negative Sp arrival in the shallow upper

763   mantle are also often zones of active or recent magmatic activity where the phase could mark the

764   base of a melt-rich mantle layer (e.g. Ford et al., 2014; Hopper et al., 2014; Rychert et al., 2018;

765   Rychert et al., 2013).

766   In contrast to many tectonically active regions with elevated mantle geotherms where a large Sp

767   arrival is observed from the base of the lithosphere (e.g. Fischer et al., 2010; Hansen et al., 2015;

768   Hopper & Fischer, 2018), in Anatolia a strong and ubiquitous phase from the LAB depth range is

769   not evident in the Sp CCP stack obtained with the 4-100 s bandpass filter. In some locations,

770   weak and vertically localized positive Sp phases representing negative velocity gradients are

771   observed directly beneath the Moho (e.g. ~30°E and 38°E in Figure 11a) but they are absent in

772   other areas (e.g. ~28°E in Figure 11a). However, when we instead applied a 2-20 s bandpass

773   filter before deconvolution, stronger and more continuous LAB phases are observed beneath the

774   Moho across most of the Anatolian region at around 60-90 km depth (Figures 16a, S6 & S7).

775   This depth range approximately corresponds to the top of the low velocity asthenosphere layer

776   (e.g. Figures 13 & S4). This observation of a shallow LAB phase is consistent with the depth of

777   the LAB in Kind et al. (2015), but unlike Kind et al. (2015), we observed the strong LAB phase

778   only at relatively short periods. In addition, the relative amplitude of the LAB phases in this

779   study is low compared to those in Kind et al. (2015), where LAB phase amplitudes are

780   sometimes comparable to Moho phases.

781   A possible reason for LAB phases to be weak or absent when using 4-100 s filter is that the

782   mantle lithosphere is too thin to be resolved by long wavelength body waves. In other words, the

783   LAB phase is reduced by interference with a larger Moho phase. To test this hypothesis, a

784   numerical experiment was designed with propagator matrix synthetic seismograms. For velocity

785   structures with varying mantle lithospheric thicknesses (Figure 17a), synthetic S waves with the

786   same ray parameter (0.1098 s/km) were recorded by a station at the surface. However, some

787   waves had Gaussian first derivative source time functions with a period of 14 s (~0.07 Hz), while

788   the others had dominant periods of 4 s (0.25 Hz), and bandpass filters of 4-100 s and 2-20 s were

789   applied. Synthetic seismograms were then deconvolved to obtain Sp receiver functions, using

790   the same approach that was applied to the data, and receiver functions were migrated to depth

791   (Figure 17a). When the mantle lithosphere is thinner than 10 km, LAB phases can barely be

792   observed for any filter or dominant period. When mantle lithosphere thickness is more than 10

793   km but less than 30 km, receiver functions with 4 s source time functions better capture LAB

794   phases with correct depths and stronger amplitudes. When mantle lithosphere thickness is

795   approximately 30 km, 4 s and 14 s receiver functions are similar. These synthetic tests indicate

796   that higher frequency seismograms better resolve LAB phases when mantle lithosphere is thin.

797   When using a 4-100 s bandpass filter with real data, S phases with periods even longer than 14 s

798   are also included, making the LAB even more difficult to observe than in the numerical

799   experiment. The 2-20 s bandpass filter does not significantly alter receiver functions with short-

800   period source time functions compared to the 4-100 s bandpass filter (e.g. middle-right versus

801   middle-left panel in Figure 17a), but it eliminates longer period waveforms that obscure the LAB

802   phase.

803   However, while the observed LAB phases become more prominent when using 2-20 s filter, the

804   positive velocity gradient phases are relatively weaker with this filter compared to the 4-100 s

805   bandpass (e.g. Figure 16a versus Figure 11a). To better understand this frequency dependence,

806   another synthetic experiment was designed with a similar setup to the former case, but with a

807   lithospheric thickness fixed at 15 km, and a shear velocity increase from 4.0 km/s to 4.4 km/s

808   centered at 120 km depth. The latter is distributed over a depth range as narrow as 10 km and as

809   broad as 45 km (Figure 17b). When a 4-100 s bandpass filter was applied, receiver functions

810   from a 4 s source time functions are more sensitive to the depth range of the velocity increase

811   when the depth range is more than 30 km, while the 14 s receiver functions show less amplitude

812   variation (middle-left versus left-most panel in Figure 17b). However, when a 2-20 s filter was

813   applied, positive velocity gradient phases become much weaker for 4 s receiver functions from

814   velocity gradients broader than 30 km (middle-right versus middle-left panel in Figure 17b).

815   This result is because the long period Green's functions for converted waves originating from the

816   gradual velocity increase are filtered out.

817   Based on this synthetic test, and the larger amplitude of the observed positive phase from the

818   base of the asthenosphere with the 4-100 s filter relative to the 2-20 s, we conclude that the

819   corresponding positive velocity gradient is likely distributed over a depth extent of at least 30

820   km. However, if the velocity gradient is distributed over more than 30 km, the synthetics

821   indicate that the amplitude of the phase should continue to increase as the dominant period in the

822   waveforms further increases, for example the 14 s source versus the 4 s source with the 4-100 s

823   filter (middle-left versus left-most panel in Figure 17b). To produce a shift to longer dominant

824   periods, we also performed the CCP stacking with Sp receiver functions from seismograms with

825   a 10-100 s bandpass filter (Figure 16b, S8 & S9). The positive velocity gradient phase in this

826   case is in many places stronger than in the 4-100 s case, especially for profile B-B' (Figure S8a

827   versus Figure 14a), suggesting that the velocity gradient is probably more gradual than a 30 km

828   depth extent.

829   These synthetic tests show that in order to observe both thin mantle lithosphere and the gradual

830   positive velocity gradient at the base of the low velocity asthenospheric layer, the best choice is

831   to use seismograms with short-period source time functions and filter them with broad bandpass

832   filters (e.g. the cases with a 4 s source time function and a 4-100 s filter in Figure 17). However,

833   with real data, a shorter period filter is often necessary to isolate short period source time

834   function seismograms, and it is key to construct receiver function stacks with different frequency

835   bands to resolve thin layers and velocity gradient depth ranges.

836

837   **5. Conclusions**

838   A new approach to finding free-surface velocities from the polarizations of P and S arrivals was

839   developed. This approach has the ability to accurately measure the shear velocity from P arrivals

840   and compressional velocity from S arrivals both with synthetic data and real data. With the

841   retrieved free-surface velocities, P and SV components of seismograms are isolated successfully,

842   resulting in clear Sp receiver functions.

843   Receiver functions were accurately mapped to depth with a novel kernel-based CCP stacking

844   method. Instead of using empirically defined weighting functions or geographic bins, the new

845   method focuses imaging the horizontal discontinuities assumed in CCP stacking using the shape

846   of scattering kernels. Receiver function amplitudes are projected into the stack using weighting

847   functions that highlight locations where the kernel is relatively flat, its depth offset from the

848   conversion point is minimal, and geometric spreading is small. With typical upper mantle

849   seismic velocities, Sp weighting functions span much broader horizontal regions than Ps

850   weighting functions, indicating an advantage for Sp receiver functions when imaging quasi-

851   horizontal structures.

852   A fast and accurate approach to quantifying the standard deviation of CCP stacking results is

853   derived based on the central limit theorem. The estimated standard deviation requires only one

854   quick calculation, but is very close to the value obtained by bootstrapping after the latter

855   converges over thousands of iterations. The derived expression can be applied to all problems

856   requiring a standard deviation of weighted averages, and it requires neither the sum of weights to

857   be constant nor the weight to be independent of the sample.

858   Sp receiver function CCP stacking, after careful quality control, resulted in clear images of upper

859   mantle discontinuities beneath the Anatolian region. Using waveforms with periods of 4-100 s,

860   the Moho, the 410-discontinuity, a velocity decrease at depths of 360-380 km, and a prominent

861   positive velocity gradient located between 80 and 150 km depth are observed. The latter positive

862   velocity gradient marks the base of a low velocity asthenospheric layer which appears in

863   numerous prior models of the Anatolian upper mantle. Causes of the pronounced low velocity

864   asthenosphere could be high mantle temperature or the presence of partial melt, which are also

865   indicated by previous geochemical and seismological studies. While the strong positive velocity

866   gradient is observed beneath most of the region, it does not extend far beyond the North

867   Anatolian Fault in western and central-eastern Anatolia, suggesting a relationship between the

868   plate boundary and its hot underlying asthenospheric mantle.

869   Strong Sp phases from a negative velocity gradient that corresponds to the LAB are not clearly

870   observed in the CCP stack that employed receiver functions with a 4-100 s bandpass filters, but

871   an LAB Sp phase was clearly imaged at 60 to 90 km depth with a 2-20 s filter. Tests with

872   synthetic seismograms show that this frequency dependent behavior is expected with thin mantle

873   lithosphere. This phase is consistent with the upper margin of the low velocity asthenosphere.

874   Frequency dependence in the amplitude of the Sp phases from the base of the asthenospheric low

875   velocity layer places constraints on the depth extent of its velocity gradient. The Sp phase

876   amplitude is clearly smallest in the CCP stack with the 2-20 s bandpass filter, indicating that the

877   positive velocity gradient occurs over more than 30 km in depth. Beneath much of the region,

878   southern portions of western and central Anatolia in particular, the amplitude of the phase is

879 larger in the CCP stack with a 10-100 s bandpass filter relative to the stack with the 4-100 s

880 bandpass filter, indicating that the depth extent of the velocity gradient is even larger.

898

References

900 Abgarmi, B., Delph, J. R., Ozacar, A. A., Beck, S. L., Zandt, G., Sandvol, E., et al. (2017). Structure of the crust and
901 African slab beneath the central Anatolian plateau from receiver functions: New insights on isostatic
902 compensation and slab dynamics. *Geosphere, 13*(6), 1774-1787. https://doi.org/10.1130/GES01509.1
903 Abt, D. L., Fischer, K. M., French, S. W., Ford, H. A., Yuan, H., & Romanowicz, B. (2010). North American
904 lithospheric discontinuity structure imaged by Ps and Sp receiver functions. *Journal of Geophysical
905 Research: Solid Earth, 115*(B9). https://doi.org/10.1029/2009JB006914
906 Aki, K., & Richards, P. G. (2002). *Quantitative seismology* (2nd ed.): University Science Books.
907 Angus, D., Wilson, D. C., Sandvol, E., & Ni, J. (2006). Lithospheric structure of the Arabian and Eurasian collision
908 zone in eastern Turkey from S-wave receiver functions. *Geophysical Journal International, 166*(3), 1335-
909 1346. https://doi.org/10.1111/j.1365-246X.2006.03070.x
910 Bakırcı, T., Yoshizawa, K., & Özer, M. F. (2012). Three-dimensional S-wave structure of the upper mantle beneath
911 Turkey from surface wave tomography. *Geophysical Journal International, 190*(2), 1058-1076.
912 https://doi.org/10.1111/j.1365-246X.2012.05526.x

913 Berk Biryol, C., Beck, S. L., Zandt, G., & Özacar, A. A. (2011). Segmented African lithosphere beneath the
914   Anatolian region inferred from teleseismic P-wave tomography. *Geophysical Journal International, 184*(3),
915   1037-1057. https://doi.org/10.1111/j.1365-246X.2010.04910.x
916 Blom, N., Gokhberg, A., & Fichtner, A. (2020). Seismic waveform tomography of the Central and Eastern
917   Mediterranean upper mantle. *Solid Earth, 11*(2), 669-690. https://doi.org/10.5194/se-11-669-2020
918 Bostock, M. G., & Rondenay, S. (1999). Migration of scattered teleseismic body waves. *Geophysical Journal
919   International, 137*(3), 732-746. https://doi.org/10.1046/j.1365-246x.1999.00813.x
920 Bostock, M. G., Rondenay, S., & Shragge, J. (2001). Multiparameter two-dimensional inversion of scattered
921   teleseismic body waves 1. Theory for oblique incidence. *Journal of Geophysical Research Solid Earth,
922   106*(B12), 30771-30782. https://doi.org/10.1029/2001JB000330
923 Crameri, F. (2018). Geodynamic diagnostics, scientific visualisation and StagLab 3.0. *Geoscientific Model
924   Development, 11*(6), 2541-2562. https://doi.org/10.5194/gmd-11-2541-2018
925 Delph, J. R., Biryol, C. B., Beck, S. L., Zandt, G., & Ward, K. M. (2015). Shear wave velocity structure of the
926   Anatolian Plate: anomalously slow crust in southwestern Turkey. *Geophysical Journal International,
927   202*(1), 261-276. https://doi.org/10.1093/gji/ggv141
928 Dueker, K. G., & Sheehan, A. F. (1997). Mantle discontinuity structure from midpoint stacks of converted P to S
929   waves across the Yellowstone hotspot track. *Journal of Geophysical Research: Solid Earth, 102*(B4), 8313-
930   8327.
931 Faccenna, C., Bellier, O., Martinod, J., Piromallo, C., & Regard, V. (2006). Slab detachment beneath eastern
932   Anatolia: A possible cause for the formation of the North Anatolian fault. *Earth and Planetary Science
933   Letters, 242*(1-2), 85-97. https://doi.org/10.1016/j.epsl.2005.11.046
934 Farra, V., & Vinnik, L. (2000). Upper mantle stratification by P and S receiver functions. *Geophysical Journal
935   International, 141*(3), 699-712. https://doi.org/10.1046/j.1365-246x.2000.00118.x
936 Fichtner, A., Saygin, E., Taymaz, T., Cupillard, P., Capdeville, Y., & Trampert, J. (2013). The deep structure of the
937   North Anatolian Fault Zone. *Earth and Planetary Science Letters, 373*, 109-117.
938   https://doi.org/10.1016/j.epsl.2013.04.027
939 Fischer, K. M., Ford, H. A., Abt, D. L., & Rychert, C. A. (2010). The lithosphere-asthenosphere boundary. *Annual
940   Review of Earth and Planetary Sciences, 38*, 551-575. https://doi.org/10.1146/annurev-earth-040809-
941   152438
942 Ford, H. A., Fischer, K. M., & Lekic, V. (2014). Localized shear in the deep lithosphere beneath the San Andreas
943   fault system. *Geology, 42*(4), 295-298. https://doi.org/10.1130/G35128.1
944 Frederiksen, A. W., Thompson, D. A., Rost, S., Cornwell, D. G., Gülen, L., Houseman, G. A., et al. (2015). Crustal
945   thickness variations and isostatic disequilibrium across the North Anatolian Fault, western Turkey.
946   *Geophysical Research Letters, 42*(3), 751-757. https://doi.org/10.1002/2014GL062401
947 Gans, C. R., Beck, S. L., Zandt, G., Biryol, C. B., & Ozacar, A. A. (2009). Detecting the limit of slab break-off in
948   central Turkey: new high-resolution Pn tomography results. *Geophysical Journal International, 179*(3),
949   1566-1572. https://doi.org/10.1111/j.1365-246X.2009.04389.x
950 Gök, R., Sandvol, E., Türkelli, N., Seber, D., & Barazangi, M. (2003). Sn attenuation in the Anatolian and Iranian
951   plateau and surrounding regions. *Geophysical Research Letters, 30*(24).
952   https://doi.org/10.1029/2003GL018020
953 Govers, R., & Fichtner, A. (2016). Signature of slab fragmentation beneath Anatolia from full-waveform
954   tomography. *Earth and Planetary Science Letters, 450*, 10-19. https://doi.org/10.1016/j.epsl.2016.06.014
955 Hannemann, K., Krüger, F., Dahm, T., & Lange, D. (2016). Oceanic lithospheric S-wave velocities from the
956   analysis of P-wave polarization at the ocean floor. *Geophysical Supplements to the Monthly Notices of the
957   Royal Astronomical Society, 207*(3), 1796-1817. https://doi.org/10.1093/gji/ggw342
958 Hansen, S. M., Dueker, K., & Schmandt, B. (2015). Thermal classification of lithospheric discontinuities beneath
959   USArray. *Earth and Planetary Science Letters, 431*, 36-47. https://doi.org/10.1016/j.epsl.2015.09.009
960 Hansen, S. M., & Schmandt, B. (2017). P and S wave receiver function imaging of subduction with scattering
961   kernels. *Geochemistry, Geophysics, Geosystems, 18*(12), 4487-4502.
962   https://doi.org/10.1002/2017GC007120
963 Hopper, E., & Fischer, K. M. (2018). The changing face of the lithosphere-asthenosphere boundary: Imaging
964   continental scale patterns in upper mantle structure across the contiguous US with Sp converted waves.
965   *Geochemistry, Geophysics, Geosystems, 19*(8), 2593-2614. https://doi.org/10.1029/2018GC007476
966 Hopper, E., Ford, H. A., Fischer, K. M., Lekic, V., & Fouch, M. J. (2014). The lithosphere–asthenosphere boundary
967   and the tectonic and magmatic history of the northwestern United States. *Earth and Planetary Science
968   Letters, 402*, 69-81. https://doi.org/10.1016/j.epsl.2013.12.016

969 Hosseini, K., & Sigloch, K. (2017). obspyDMT: a Python toolbox for retrieving and processing of large
970   seismological datasets. *Solid Earth, 8*. https://doi.org/10.5194/se-8-1047-2017
971 Hua, J., Fischer, K. M., Mancinelli, N. J., & Bao, T. (2020). Imaging with pre-stack migration based on Sp
972   scattering kernels. *Geophysical Journal International, 220*(1), 428-449. https://doi.org/10.1093/gji/ggz459
973 Hua, J., Fischer, K. M., & Savage, M. K. (2018). The lithosphere–asthenosphere boundary beneath the South Island
974   of New Zealand. *Earth and Planetary Science Letters, 484*, 92-102.
975   https://doi.org/10.1016/j.epsl.2017.12.011
976 Jolivet, L., Faccenna, C., Huet, B., Labrousse, L., Le Pourhiet, L., Lacombe, O., et al. (2013). Aegean tectonics:
977   Strain localisation, slab tearing and trench retreat. *Tectonophysics, 597-598*, 1-33.
978   https://doi.org/10.1016/j.tecto.2012.06.011
979 Kandilli Observatory and Earthquake Research Institute Bosphorus Univ. (2001). *Bogazici University Kandilli*
980   *Observatory And Earthquake Research Institute*. International Federation of Digital Seismograph
981   Networks. Dataset/Seismic Network.
982 Karabulut, H., Paul, A., Özbakır, A. D., Ergün, T., & Şentürk, S. (2019). A new crustal model of the Anatolia–
983   Aegean domain: evidence for the dominant role of isostasy in the support of the Anatolian plateau.
984   *Geophysical Journal International, 218*(1), 57-73. https://doi.org/10.1093/gji/ggz147
985 Keith, C. M., & Crampin, S. (1977). Seismic body waves in anisotropic media: synthetic seismograms. *Geophysical*
986   *Journal International, 49*(1), 225-243.
987 Kennett, B. L. (1991). The removal of free surface interactions from three-component seismograms. *Geophysical*
988   *Journal International, 104*(1), 153-154. https://doi.org/10.1111/j.1365-246X.1991.tb02501.x
989 Kennett, B. L., Engdahl, E., & Buland, R. (1995). Constraints on seismic velocities in the Earth from traveltimes.
990   *Geophysical Journal International, 122*(1), 108-124. https://doi.org/10.1111/j.1365-246X.1995.tb03540.x
991 Keskin, M. (2003). Magma generation by slab steepening and breakoff beneath a subduction-accretion complex: An
992   alternative model for collision-related volcanism in Eastern Anatolia, Turkey. *Geophysical Research*
993   *Letters, 30*(24). https://doi.org/10.1029/2003GL018019
994 Kind, R., Eken, T., Tilmann, F., Sodoudi, F., Taymaz, T., Bulut, F., et al. (2015). Thickness of the lithosphere
995   beneath Turkey and surroundings from S-receiver functions. *Solid Earth, 6*(3), 971-984.
996   https://doi.org/10.5194/se-6-971-2015
997 Kind, R., Yuan, X., & Kumar, P. (2012). Seismic receiver functions and the lithosphere–asthenosphere boundary.
998   *Tectonophysics, 536*, 25-43. https://doi.org/10.1016/j.tecto.2012.03.005
999 Lekić, V., & Fischer, K. M. (2014). Contrasting lithospheric signatures across the western United States revealed by
1000   Sp receiver functions. *Earth and Planetary Science Letters, 402*, 90-98.
1001   https://doi.org/10.1016/j.epsl.2013.11.026
1002 Lekić, V., & Fischer, K. M. (2017). Interpreting spatially stacked Sp receiver functions. *Geophysical Journal*
1003   *International, 210*(2), 874-886. https://doi.org/10.1093/gji/ggx206
1004 Lekic, V., French, S. W., & Fischer, K. M. (2011). Lithospheric thinning beneath rifted regions of southern
1005   California. *Science, 334*(6057), 783-787. https://doi.org/10.1126/science.1208898
1006 Licciardi, A., Eken, T., Taymaz, T., Agostinetti, N. P., & Yolsal-Çevikbilen, S. (2018). Seismic anisotropy in central
1007   North Anatolian Fault Zone and its implications on crustal deformation. *Physics of the Earth and Planetary*
1008   *Interiors, 277*, 99-112. https://doi.org/10.1016/j.pepi.2018.01.012
1009 Ligorria, J. P., & Ammon, C. J. (1999). Iterative deconvolution and receiver-function estimation. *Bulletin of the*
1010   *seismological Society of America, 89*(5), 1395-1400.
1011 Mancinelli, N., & Fischer, K. (2017). The spatial sensitivity of Sp converted waves—scattered-wave kernels and
1012   their applications to receiver-function migration and inversion. *Geophysical Journal International, 212*(3),
1013   1722-1735. https://doi.org/10.1093/gji/ggx506
1014 McNab, F., Ball, P. W., Hoggard, M. J., & White, N. J. (2018). Neogene Uplift and Magmatism of Anatolia:
1015   Insights From Drainage Analysis and Basaltic Geochemistry. *Geochemistry, Geophysics, Geosystems,*
1016   *19*(1), 175-213. https://doi.org/10.1002/2017GC007251
1017 Mutlu, A. K., & Karabulut, H. (2011). Anisotropic Pn tomography of Turkey and adjacent regions. *Geophysical*
1018   *Journal International, 187*(3), 1743-1758. 10.1111/j.1365-246X.2011.05235.x
1019 Nikogosian, I., Gartner, A. B., van Bergen, M., Mason, P., & Van Hinsbergen, D. J. (2018). Mantle sources of
1020   recent Anatolian intraplate magmatism: A regional plume or local tectonic origin? *Tectonics, 37*(12), 4535-
1021   4566. https://doi.org/10.1029/2018TC005219
1022 Ozacar, A. A., Gilbert, H., & Zandt, G. (2008). Upper mantle discontinuity structure beneath East Anatolian Plateau
1023   (Turkey) from receiver functions. *Earth and Planetary Science Letters, 269*(3-4), 427-435.
1024   https://doi.org/10.1016/j.epsl.2008.02.036

Park, S., & Ishii, M. (2018). Near-surface compressional and shear wave speeds constrained by body-wave polarization analysis. *Geophysical Journal International, 213*(3), 1559-1571. https://doi.org/10.1093/gji/ggy072

Park, S., Tsai, V. C., & Ishii, M. (2019). Frequency-Dependent P Wave Polarization and Its Subwavelength Near-Surface Depth Sensitivity. *Geophysical Research Letters*. https://doi.org/10.1029/2019GL084892

Portner, D. E., Delph, J. R., Biryol, C. B., Beck, S. L., Zandt, G., Özacar, A. A., et al. (2018). Subduction termination through progressive slab deformation across Eastern Mediterranean subduction zones from updated P-wave tomography beneath Anatolia. *Geosphere, 14*(3), 907-925. https://doi.org/10.1130/GES01617.1

Reid, M. R., Schleiffarth, W. K., Cosca, M. A., Delph, J. R., Blichert-Toft, J., & Cooper, K. M. (2017). Shallow melting of MORB-like mantle under hot continental lithosphere, Central Anatolia. *Geochemistry, Geophysics, Geosystems, 18*(5), 1866-1888. https://doi.org/10.1002/2016GC006772

Reilinger, R., McClusky, S., Vernant, P., Lawrence, S., Ergintav, S., Cakmak, R., et al. (2006). GPS constraints on continental deformation in the Africa-Arabia-Eurasia continental collision zone and implications for the dynamics of plate interactions. *Journal of Geophysical Research: Solid Earth, 111*(B5). https://doi.org/10.1029/2005JB004051

Rondenay, S. (2009). Upper mantle imaging with array recordings of converted and scattered teleseismic waves. *Surveys in Geophysics, 30*(4-5), 377-405. https://doi.org/10.1007/s10712-009-9071-5

Rondenay, S., Bostock, M. G., & Fischer, K. M. (2005). Multichannel inversion of scattered teleseismic body waves: Practical considerations and applicability. *Washington Dc American Geophysical Union Geophysical Monograph, 157*, 187-203. https://doi.org/10.1029/157GM12

Rychert, C. A., Harmon, N., & Tharimena, S. (2018). Scattered wave imaging of the oceanic plate in Cascadia. *Science advances, 4*(2), eaao1908. https://doi.org/10.1126/sciadv.aao1908

Rychert, C. A., Laske, G., Harmon, N., & Shearer, P. M. (2013). Seismic imaging of melt in a displaced Hawaiian plume. *Nature Geoscience, 6*(8), 657-660. https://doi.org/10.1038/ngeo1878

Salaün, G., Pedersen, H. A., Paul, A., Farra, V., Karabulut, H., Hatzfeld, D., et al. (2012). High-resolution surface wave tomography beneath the Aegean-Anatolia region: constraints on upper-mantle structure. *Geophysical Journal International, 190*(1), 406-420. https://doi.org/10.1111/j.1365-246X.2012.05483.x

Schildgen, T. F., Yıldırım, C., Cosentino, D., & Strecker, M. R. (2014). Linking slab break-off, Hellenic trench retreat, and uplift of the Central and Eastern Anatolian plateaus. *Earth-Science Reviews, 128*, 147-168. https://doi.org/10.1016/j.earscirev.2013.11.006

Şengör, A., Özeren, S., Genç, T., & Zor, E. (2003). East Anatolian high plateau as a mantle-supported, north-south shortened domal structure. *Geophysical Research Letters, 30*(24). https://doi.org/10.1029/2003GL017858

Şengör, A. M. C., Özeren, M. S., Keskin, M., Sakınç, M., Özbakır, A. D., & Kayan, İ. (2008). Eastern Turkish high plateau as a small Turkic-type orogen: Implications for post-collisional crust-forming processes in Turkic-type orogens. *Earth-Science Reviews, 90*(1-2), 1-48. https://doi.org/10.1016/j.earscirev.2008.05.002

Svenningsen, L., & Jacobsen, B. (2007). Absolute S-velocity estimation from receiver functions. *Geophysical Journal International, 170*(3), 1089-1094. https://doi.org/10.1111/j.1365-246X.2006.03505.x

Vanacore, E. A., Taymaz, T., & Saygin, E. (2013). Moho structure of the Anatolian Plate from receiver function analysis. *Geophysical Journal International, 193*(1), 329-337. https://doi.org/10.1093/gji/ggs107

Vinnik, L., & Farra, V. (2002). Subcratonic low-velocity layer and flood basalts. *Geophysical Research Letters, 29*(4), 8-1-8-4. https://doi.org/10.1029/2001GL014064

Wei, W., Zhao, D., Wei, F., Bai, X., & Xu, J. (2019). Mantle Dynamics of the Eastern Mediterranean and Middle East: Constraints From P-Wave Anisotropic Tomography. *Geochemistry, Geophysics, Geosystems, 20*(10), 4505-4530. https://doi.org/10.1029/2019GC008512

Wiechert, E., & Zoeppritz, K. (1907). Über erdbebenwellen. *Nachrichten von der Gesellschaft der Wissenschaften zu Göttingen, Mathematisch-Physikalische Klasse, 1907*, 415-549.

Wittlinger, G., & Farra, V. (2007). Converted waves reveal a thick and layered tectosphere beneath the Kalahari super-craton. *Earth and Planetary Science Letters, 254*(3-4), 404-415. https://doi.org/10.1016/j.epsl.2006.11.048

Yuan, X., Kind, R., Li, X., & Wang, R. (2006). The S receiver functions: synthetics and data example. *Geophysical Journal International, 165*(2), 555-564. https://doi.org/10.1111/j.1365-246X.2006.02885.x

Zhang, H., & Schmandt, B. (2019). Application of Ps Scattering Kernels to Imaging the Mantle Transition Zone with Receiver Functions. *Journal of Geophysical Research: Solid Earth*. https://doi.org/10.1029/2018JB016274

1080 Zhu, H. (2018). High Vp/Vs ratio in the crust and uppermost mantle beneath volcanoes in the Central and Eastern
1081   Anatolia. *Geophysical Journal International, 214*(3), 2151-2163. https://doi.org/10.1093/gji/ggy253
1082 Zhu, L., Mitchell, B. J., Akyol, N., Cemen, I., & Kekovali, K. (2006). Crustal thickness variations in the Aegean
1083   region and implications for the extension of continental crust. *Journal of Geophysical Research: Solid
1084   Earth, 111*(B1). https://doi.org/10.1029/2005JB003770
1085 Zor, E., Sandvol, E., Gürbüz, C., Türkelli, N., Seber, D., & Barazangi, M. (2003). The crustal structure of the East
1086   Anatolian plateau (Turkey) from receiver functions. *Geophysical Research Letters, 30*(24).
1087   https://doi.org/10.1029/2003GL018192

1088

Figures:

1090
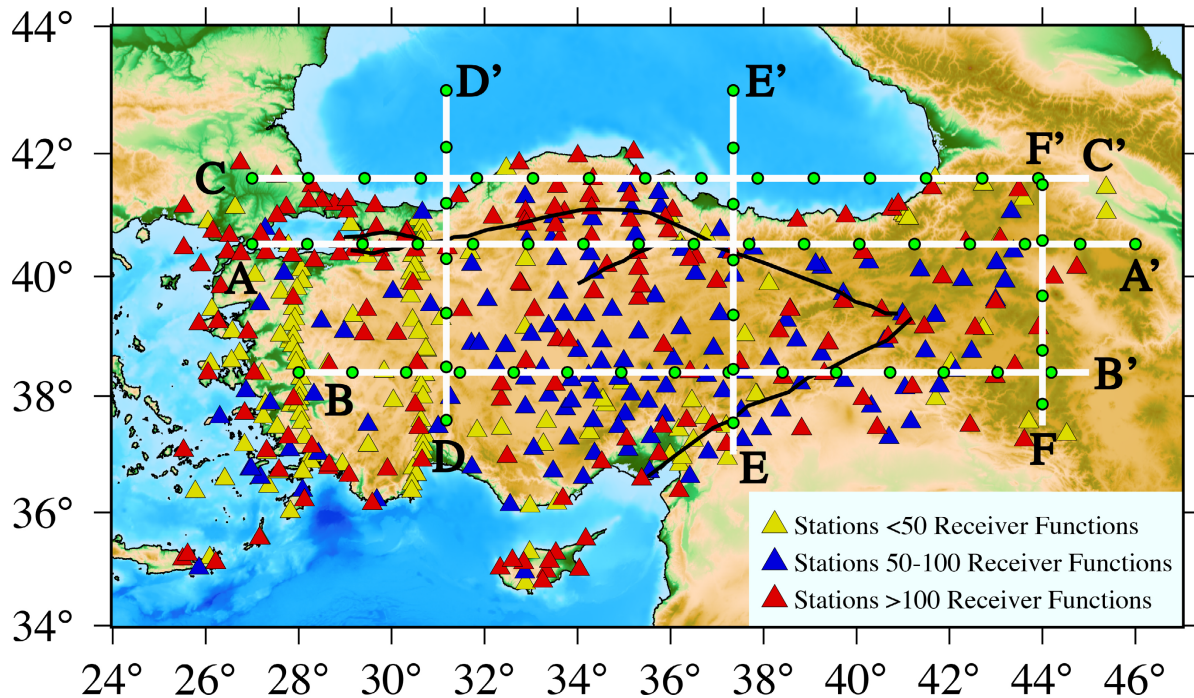
Figure 1. Map of the study region covering the Anatolian Plate. Broadband stations employed in this study are triangles; stations with less than 50 Sp receiver functions are shown in yellow color, those with 50 to 100 receiver functions are in blue, and those with more than 100 receiver functions are in red. The North Anatolian Fault and East Anatolian Fault are shown by black lines. Bold white are the locations of profiles discussed in this paper; the distance between the green circles is 100 km.

Data Acquisition	Data Pre-processing	Receiver Functions	CCP Stacking	Results
STEP 1	STEP 2	STEP 3	STEP 4	STEP 5

STEP 1
- Obtain data for the study region with suitable epicentral distances (55-85° for S and 35-80° for P). S phases are used in all later steps, including CCP stacking, P phases are used for free-surface velocity estimation.

STEP 2
- Pick P and SV arrivals based on the array-picking technique (Lekic & Fischer, 2014).
- **Measure free-surface velocities from incident phase particle motions (Section 2.1).**
- Convert radial and vertical components to P and SV components with the free surface transform.
- Window and filter the data. Estimate signal-to-noise ratios (Section 3).

STEP 3
- Calculate receiver functions between P and SV components with time domain deconvolution (Ligorria & Ammon, 1999).
- Migrate receiver functions to depth with local velocity models (Section 3).
- Quality control receiver functions based on signal-to-noise ratios and other criteria (Section 3).

STEP 4
- **Project receiver functions to 3D space with scattering kernel based CCP stacking (Section 2.2).**
- **Estimate the standard deviations of stack amplitudes with equations derived in Section 2.3.**

STEP 5
- Identify reliable phases based on the spatial sampling provided by data and stack standard deviations (Section 3).
- Analyze velocity gradients with different vertical dimensions with data filtered at different frequencies (Section 4).

1102
1103   **Figure 2.** Flow chart with the five main steps involved in calculating the Sp CCP stack.
1104   Operations shown in bold correspond to methodological improvements introduced in this study.
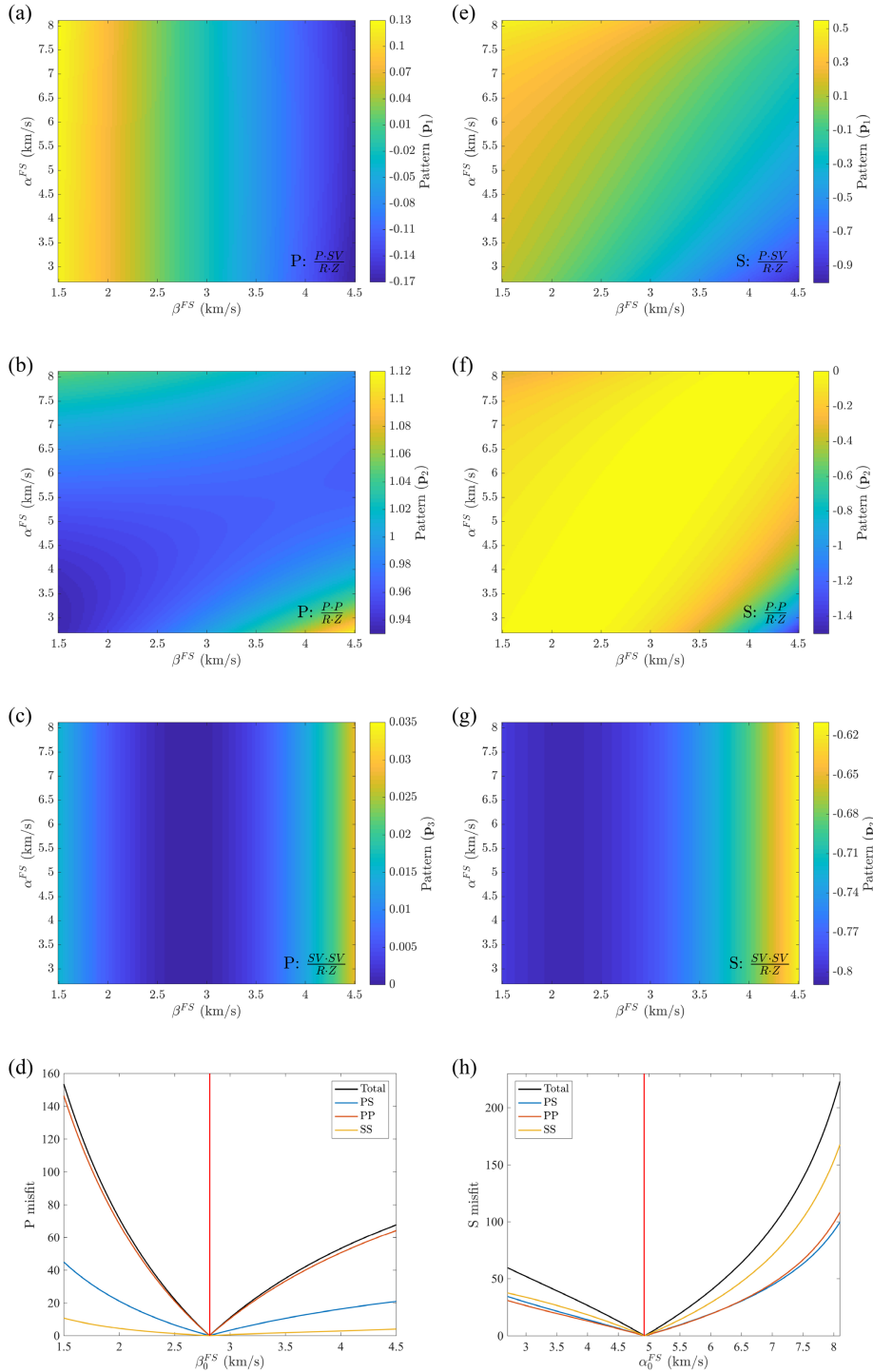
Figure 3. Particle motion patterns in equation (4) obtained with synthetic seismograms generated for a half space with V_p=4.92 km/s and V_s=2.82 km/s. (a) The pattern $\mathbf{C}_1$ in equation (4) for a P arrival with a ray parameter of 0.0482 s/km. Colors show the value of the pattern for varying α^{FS} and β^{FS}. The label at the bottom right corner indicates the arrival phase and the equation for the pattern. (b)-(c) similar to (a), but for $\mathbf{C}_2$ and $\mathbf{C}_3$. (d) Determination of β_0^{FS} by

1111   minimizing the misfit function defined in section 2.1. The black curve shows the value of the

1112   total misfit function defined in equation (6) for different β_0^{FS}, the blue curve shows the value

1113   when the misfit function is defined as $\left\|\mathbf{C}_1 - \mathbf{C}_1^p\right\|_2$, the red curve is for misfit function $\left\|\mathbf{C}_2 - \mathbf{C}_2^p\right\|_2$,

1114   and the yellow curve is for misfit function $\left\|\mathbf{C}_3 - \mathbf{C}_3^p\right\|_2$. $\mathbf{C}_2$ makes the largest contribution to the

1115   total misfit. The vertical red line shows the true β_0^{FS} from the structure used to calculate the

1116   synthetic waveforms. (e)-(g) similar to (a)-(c) but for an S-arrival with a ray parameter of 0.1098

1117   s/km. (h) similar to (d) but searching for α_0^{FS}; the vertical red line indicates the true α_0^{FS}.

1118
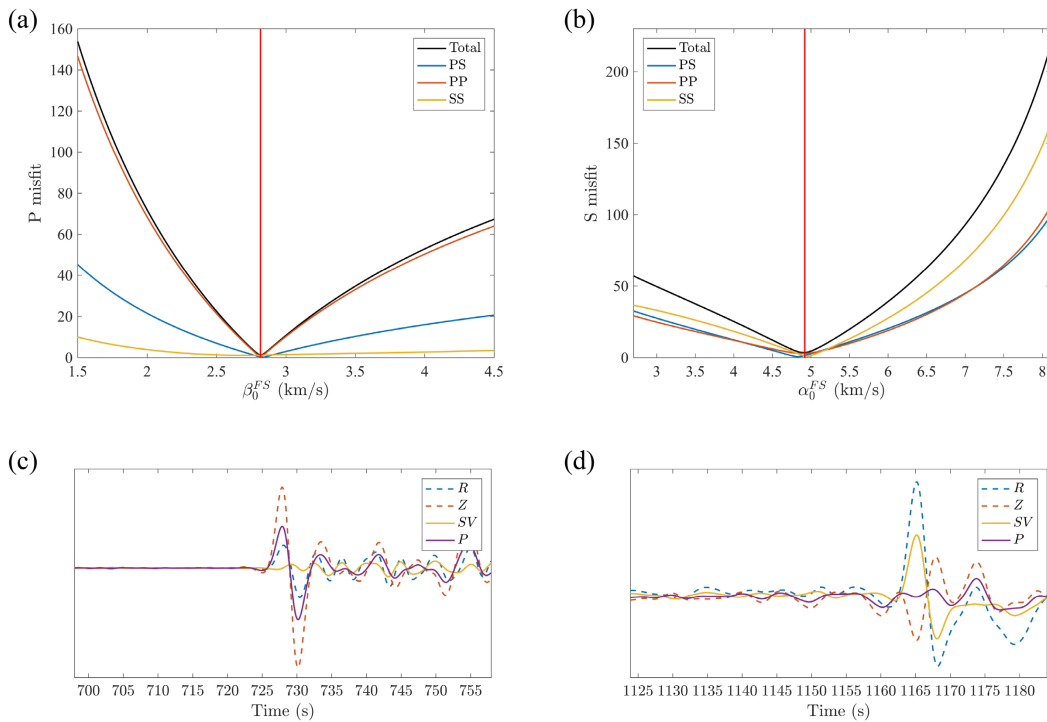
1119

1120   **Figure 4.** (a) Plot similar to Figure 3d and (b) plot similar to Figure 3h but using records from

1121   two real events. Both the P arrival event and the S arrival event have the same ray parameters as

1122   those used in the synthetic case in Figure 3. Colors and curves are defined identically to those in

1123   Figure 3. The only difference is the vertical red lines show the β_0^{FS} and α_0^{FS} values obtained by

1124   minimizing the misfit function in equation (6); their values are equal to the half space velocities

1125   used in Figure 3. (c) P and SV component example for the real P arrival used in (a). The x-axis

1126   is time from the earthquake origin time. Blue and red dashed lines show the radial and vertical

1127   components of the seismogram, and yellow and purple lines are the P and SV components based

1128   on equation (1) and the determined β_s^{FS} and α_s^{FS} values. (d) Similar to (c), but for the real S

1129   arrival used in (b).

1130
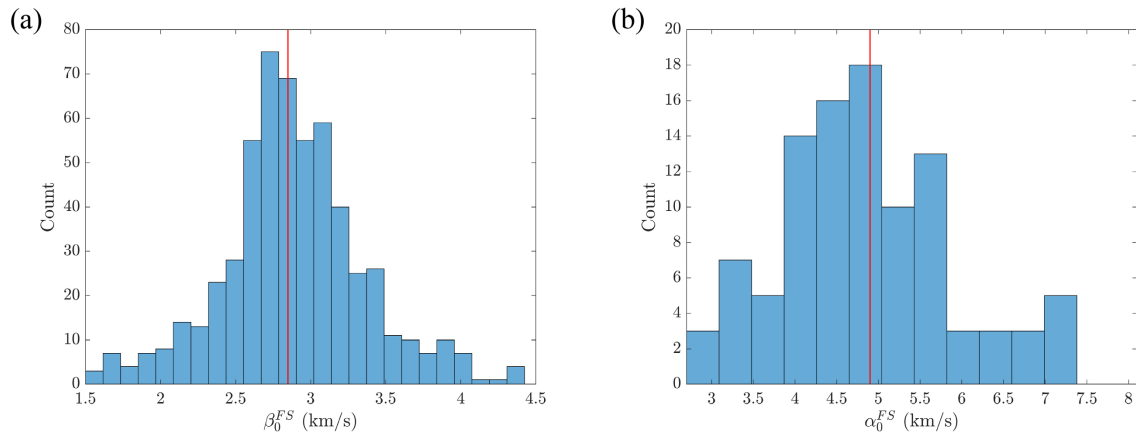
Figure 5. (a) Histogram of β_0^{FS} values obtained from 562 individual P-arrivals whose weight for free surface velocity calculation is not zero. The bin width is 0.117 km/s. The red line shows the final determined β_s^{FS} from the weighted average of individual β_0^{FS}. (b) Similar to (a) but with results for α_0^{FS} from 100 individual S-arrivals. The bin width is 0.39 km/s.
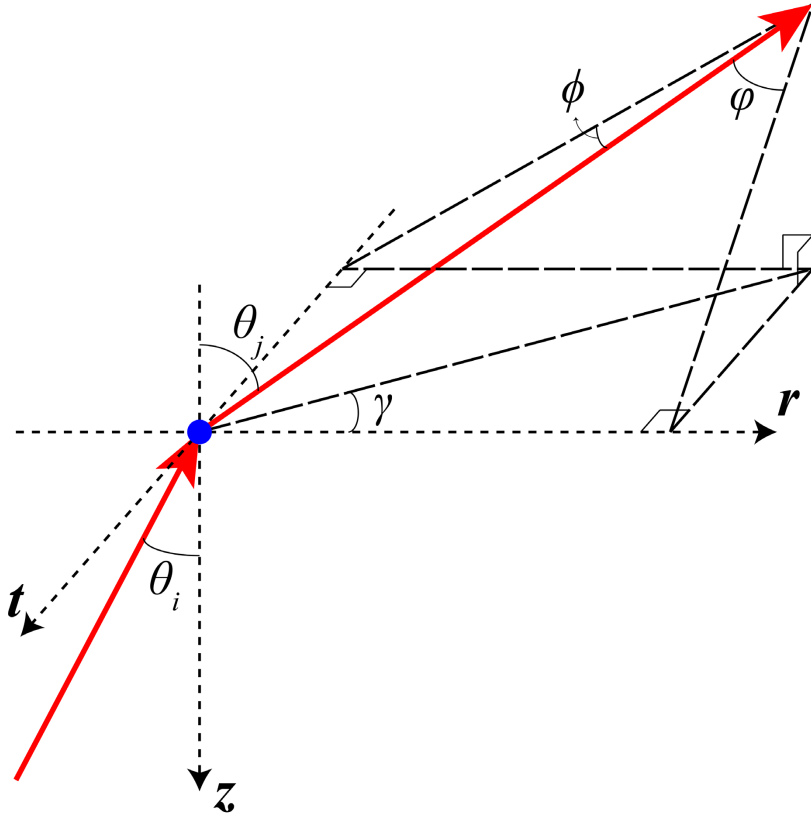
1148

1149 **Figure 6.** Schematic plot of the scattering process. Ray paths of the incident wave propagating in
1150 the *r-z* plane and the scattered wave are shown by red lines. The scatterer is marked by the blue
1151 dot. The coordinates and angles used for calculating the phase delay time isochron slope angle
1152 are also labelled.

1153
1154
1155
1156
1157
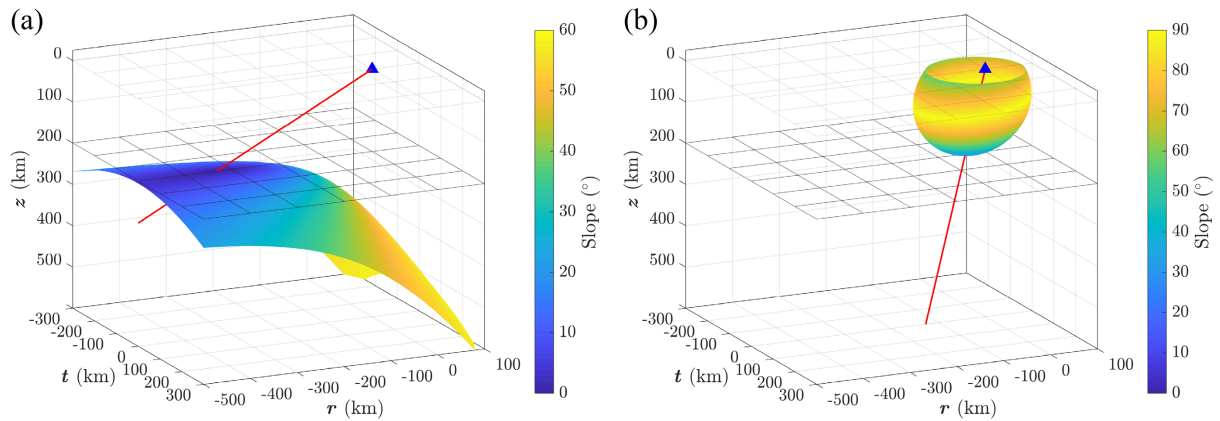
1158

Figure 7. Examples of converted phase delay time isochrons (curved surfaces) for Sp (a) and Ps (b) phases. This case is for a half space with V_p=7.8 km/s and V_s=4.3 km/s. Conversion points are at 200 km depth and ray paths are shown by red lines. The station is a blue triangle at (0 km, 0 km, 0 km). The black mesh at 200 km depth shows the horizontal plane for CCP stacking. (a) The isochron for Sp scattering, with an incident S wave ray parameter of 0.1098 s/km. Delay time for the isochron is -27.76 s. Colors on the isochron are the slope angle calculated from equation (12). (b) Similar to (a) but for Ps scattering, and an incident P wave ray parameter of 0.0482 s/km. Delay time for the isochron is 21.74 s

1167
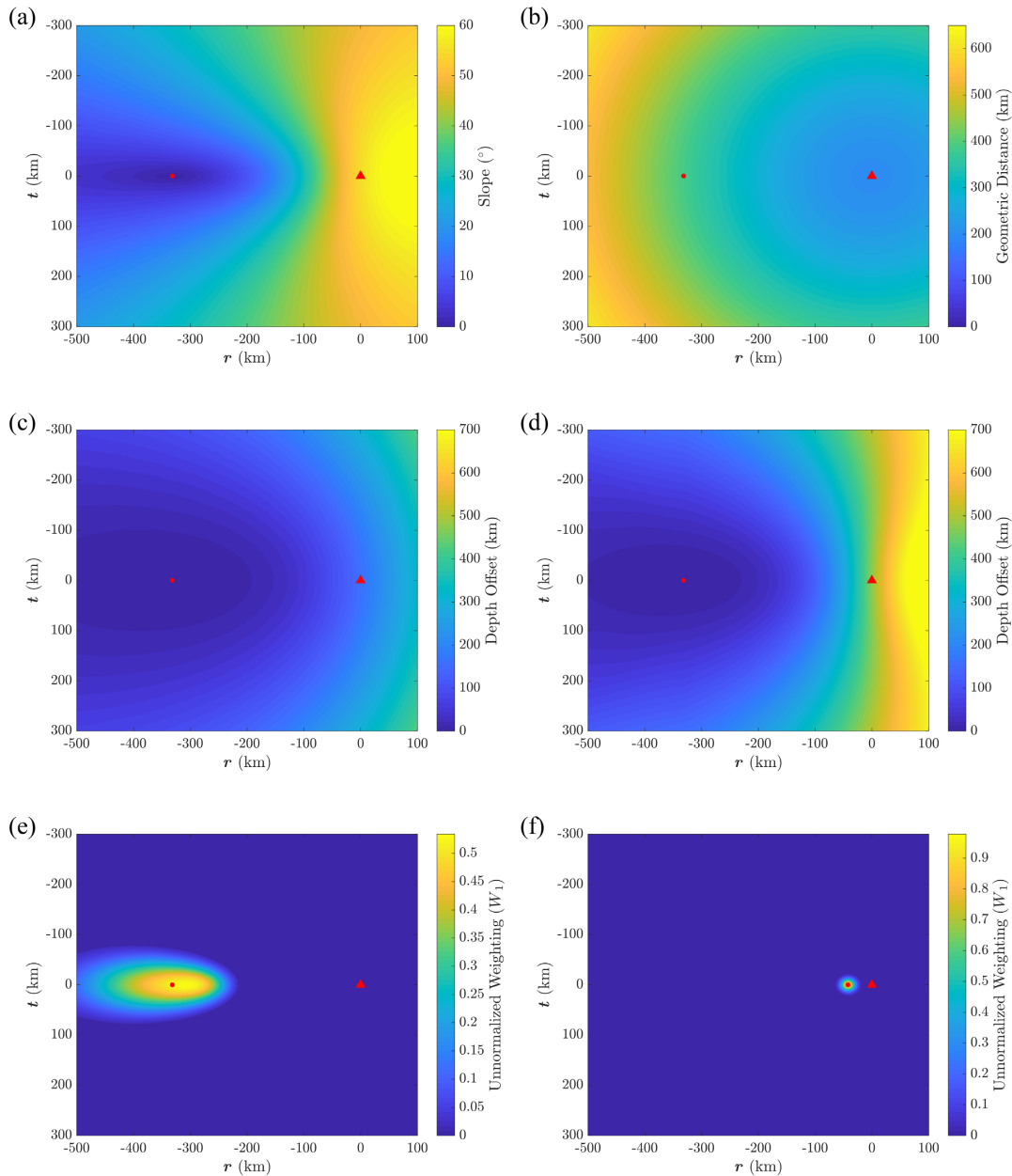
Figure 8. Properties related to the weighting function in equation (16) calculated for the same structure as used in Figure 7. (a)-(e) correspond to the Sp scattering case in Figure 7a and are for a depth of 200 km. The red circle shows the conversion point, and the triangle shows the horizontal position of the station projected downward from the surface. (a) The slope angle distribution based on equation (12). (b) The geometric distance from each point to the station. (c) The depth offset from the isochron to the stacking depth at 200 km (black mesh in Figure 7a). (d) The depth offset estimated based equation (15) which is comparable to the true depth offset in (c) near the conversion point. (e) The complete weighting function based on equation (16) that combines information in (a), (b) and (d); (f) Similar to (e), but for the Ps scattering case in Figure 7b.
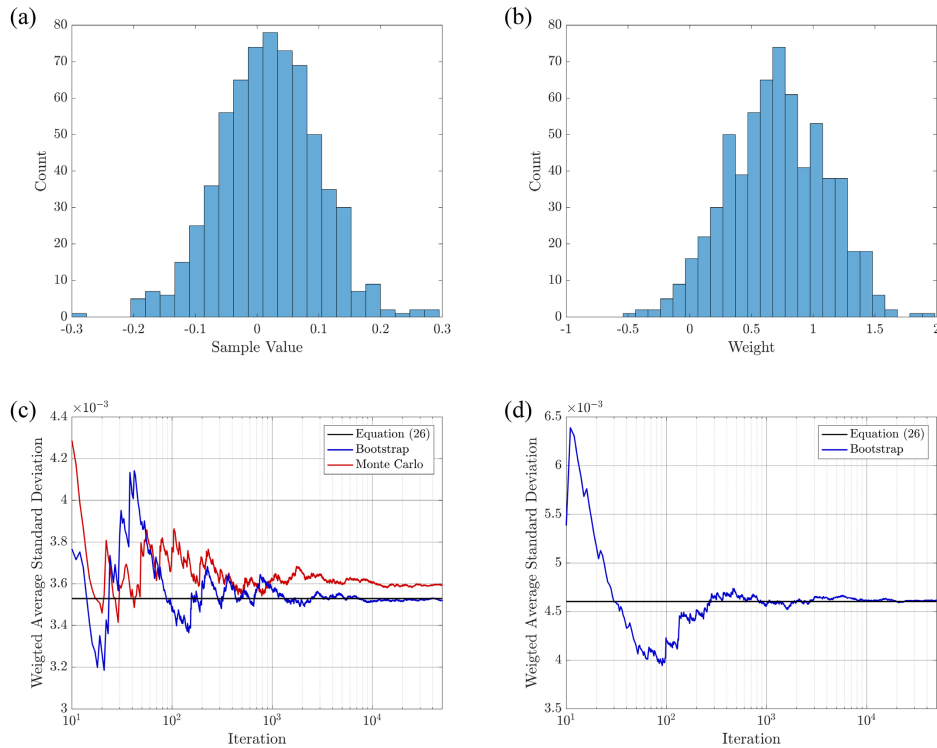
1179

Figure 9. (a) Histogram of 648 randomly generated samples from a normal distribution of $N(0.02, 0.08^2)$, and the bin width is 0.024. (b) Histogram of 648 randomly generated weights from a normal distribution of $N(0.7, 0.4^2)$, and the bin width is 0.101. (c) The standard deviation of the weighted average of the samples in (a) with weights in (b). The black line shows the standard deviation estimate from equation (26); the blue line shows the standard deviation estimate from bootstrapping, where the x-axis shows the number of bootstrap iterations; the red line shows the true standard deviation estimated from a Monte Carlo approach, where the x-axis shows the number of Monte Carlo simulations. (d) The standard deviation of the CCP stack of Anatolia receiver function amplitudes at 40.5°N, 38°E and 125 km depth; the lines have the same meaning as in (c).

1190

(a)

(b)
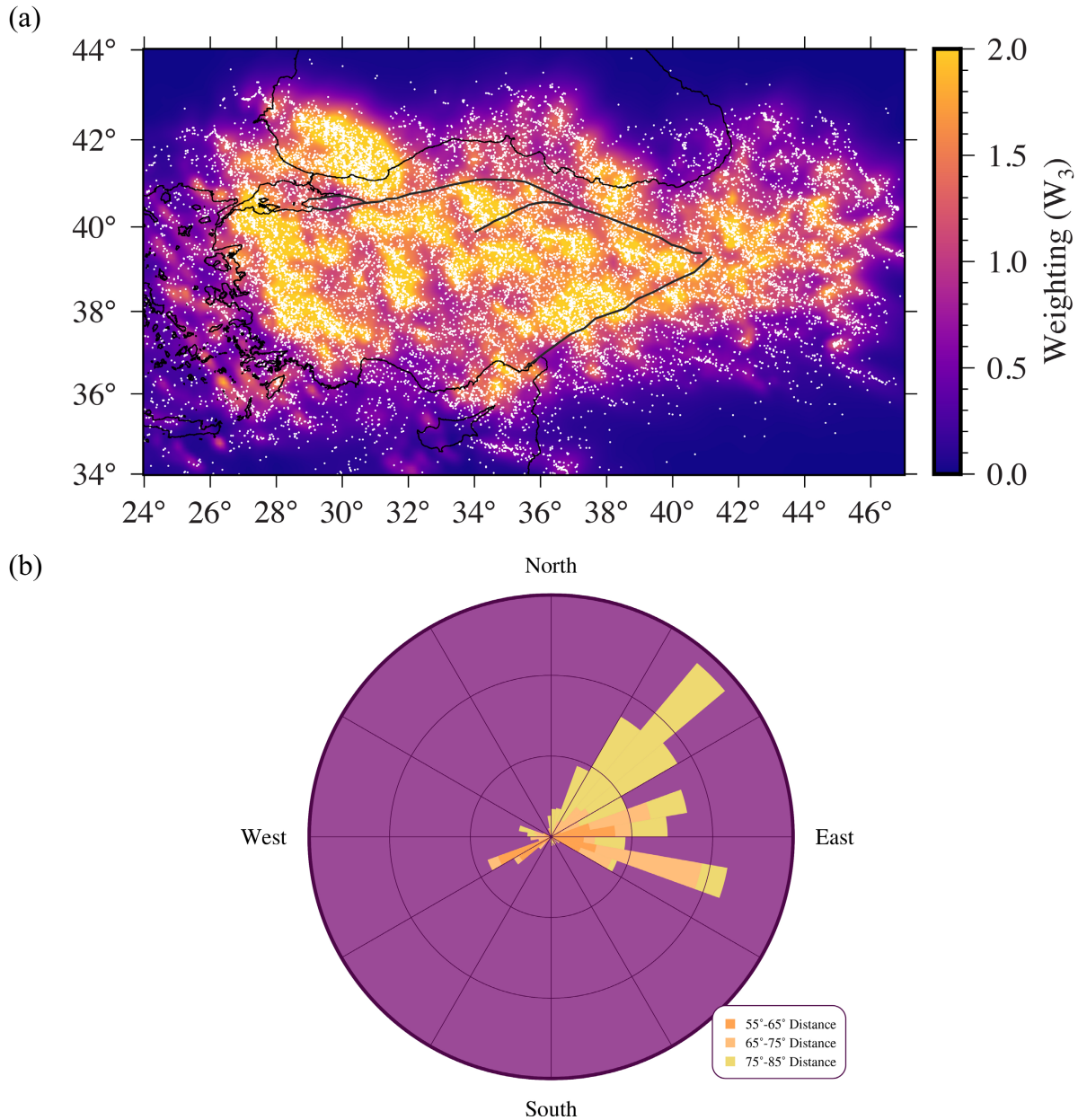
Figure 10. (a) Sp receiver function data sampling of the Anatolian region. Color shows the combined receiver function weights, W_3 (equation 27), at 125 km depth. Locations with W_3 values of more than 2.0 are shown by the yellow color that corresponds to 2.0 on the scale. White dots are piercing point locations of the 23,787 converted P wave ray paths employed in the final CCP stack. The weighting is generally stronger where piercing points are denser. (b) Back-azimuth and epicentral distance distribution for the 23,787 records. The diagram is divided into 10° back-azimuthal bins. Radial lines measure the percentage of the data that falls within a back-azimuthal bin. The maximum radius corresponds to 15%, and thin black circles mark 5% and 10%. In each back-azimuthal bin, lengths of sectors with different colors represent the proportion of earthquakes with different epicentral distance ranges as specified by the legend.
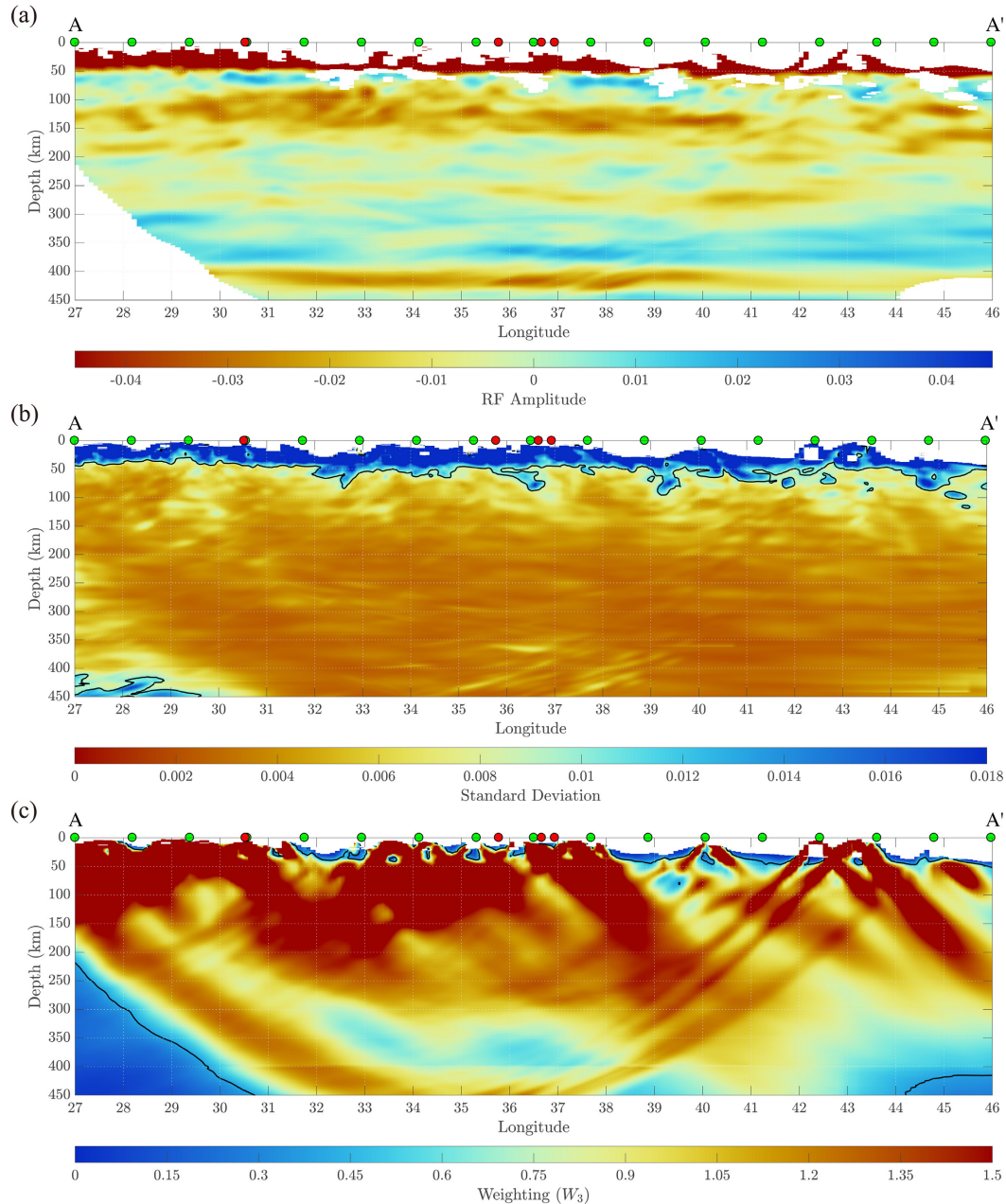
Figure 11. Properties of the Sp CCP stack shown on east-west oriented profile A-A' at 40.5°N. Horizontal axes are annotated with longitude, and vertical axes are annotated with depth. The location of the profile is shown in Figure 1. Green circles at the top of the profiles correspond to green circles on the map, with 100 km distance between them. Red circles show the intersection point of the profile with the North Anatolian Fault or East Anatolian Fault. The length of the profile is 1,603 km. (a) Sp CCP stack amplitude. Red amplitudes correspond to negative Sp phases and a velocity increase with depth (e.g. the Moho above 50 km and the 410-discontinuity); blue amplitudes correspond to positive Sp phases and a velocity decrease with depth. Phases with amplitude exceeding the limit of the color bar are shown by the boundary color (e.g. the Moho phase). Blank areas indicate zones where the image is not robust and should not be interpreted, either due to a standard deviation that exceeds both 0.01 and half of the

1214   receiver function amplitude, or due to a weight value W_3 (equation 27) that is less than 0.4. (b)

1215   The standard deviation of the Sp CCP stack amplitude from equation (26). Black line shows the

1216   contour where standard deviation equals 0.01. c) The total weight W_3. Black line shows the

1217   contour where equals 0.4. Locations with W_3 that is more than the limit of the color bar are

1218   shown by the maximum color. The color map used in this figure and all others with CCP stacks

1219   is from Crameri (2018) although with a 50% increased saturation.

1220
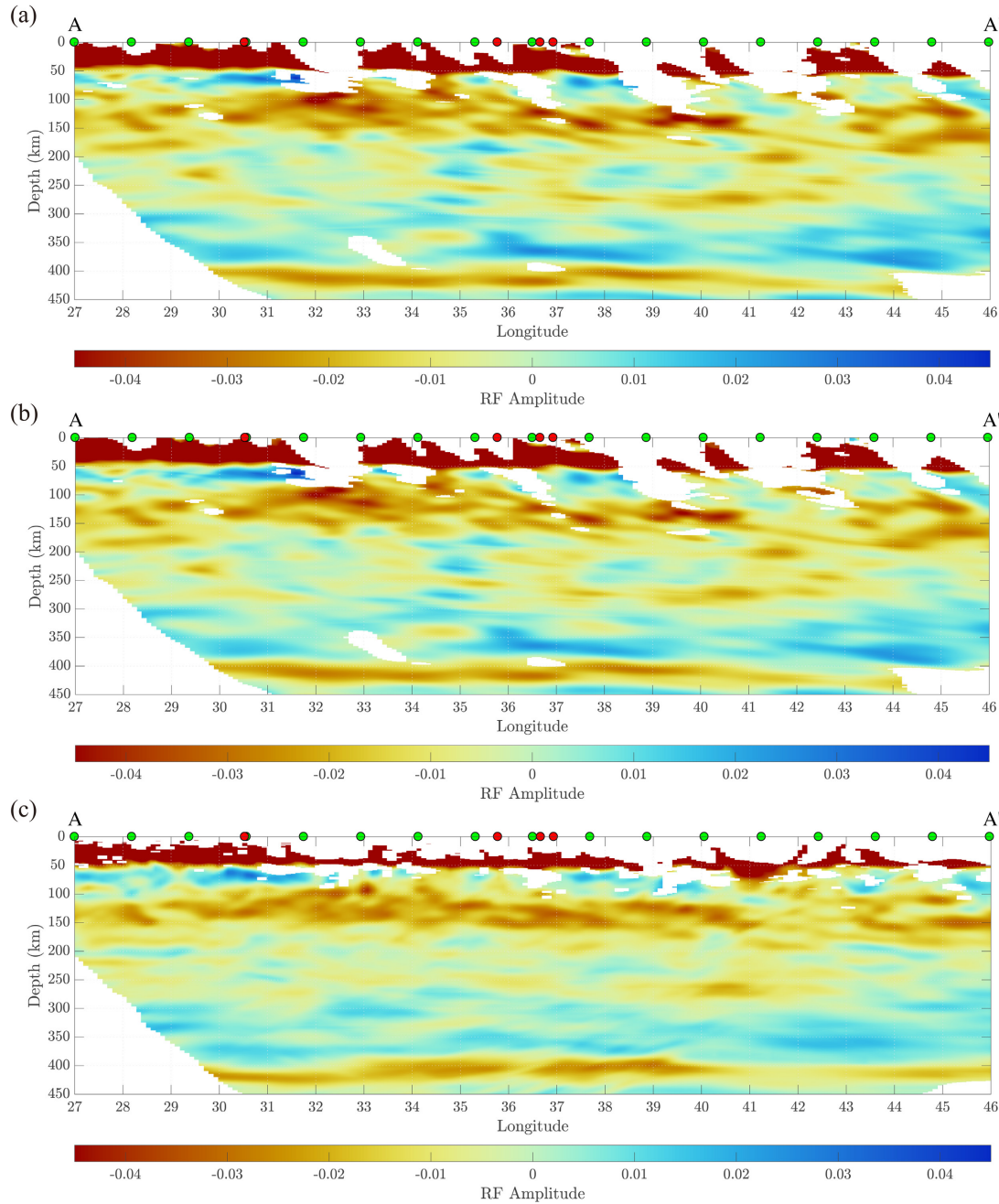
Figure 12. Sp CCP stack amplitudes on profile A-A' using different methods and velocity structures. Symbols and notations identical to Figure 11a. (a) CCP stack obtained using the empirical weighting function defined by a 13 s P wave Fresnel Zone (Lekic et al., 2011). Because the weighting function is defined differently than in Figure 11a, locations with W_3 less than 40 are blank, while the criteria for standard deviation are the same. (b) CCP stack using the free-surface velocity determination method in Abt et al. (2010), and the stacking method as in (a). Blank regions are identified identically to (a). (c) CCP stack using the methods also used in Figure 11a, except with the full-waveform inversion model of Fichtner et al. (2013). Blank regions are identified identically to Figure 11a.

1231

(a)
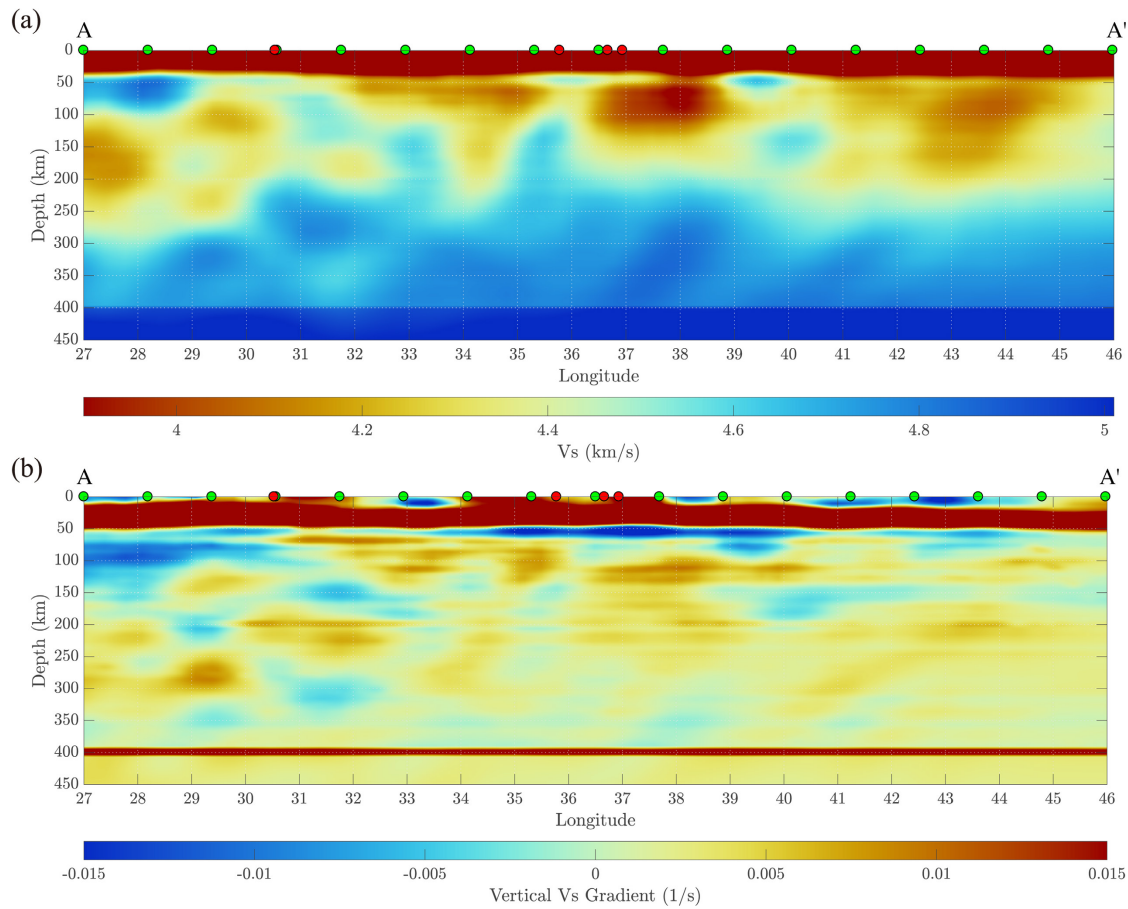
1232

Figure 13. Shear velocity model on profile A-A'. (a) Shear wave velocity from Blom et al. (2020). Velocities exceeding the limit of the color bar are shown by the color at the limit (e.g. crustal velocities). (b) Vertical gradients in shear-wave velocity from Blom et al. (2020) smoothed over a 5 km depth window.
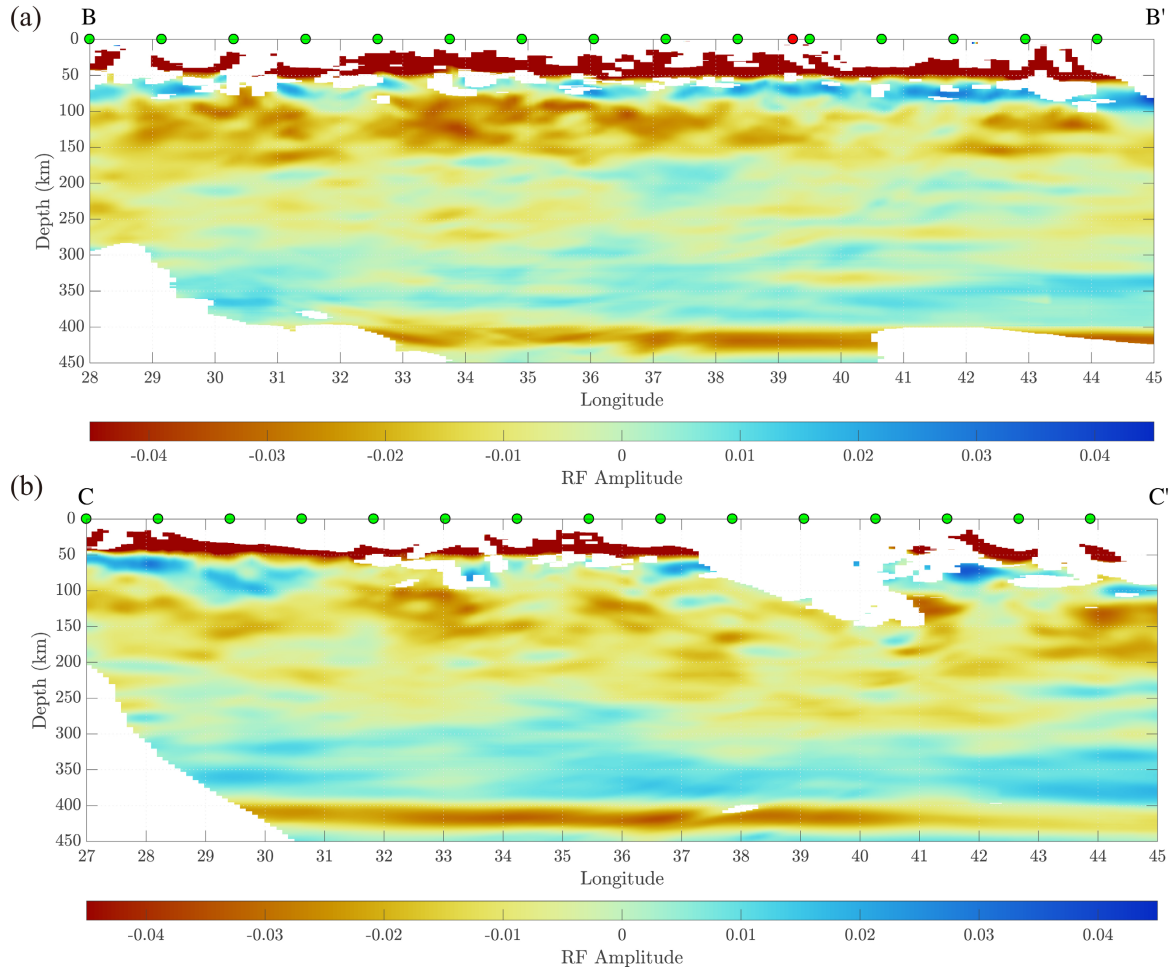
Figure 14. Sp CCP stack amplitudes on east-west profiles B-B' and C-C'. Symbols and notations identical to Figure 11a. (a) Profile B-B' is located at 38.4°N, and the length of the profile is 1,479 km. (b) Profile C-C' is located at 41.6°N, and the length of the profile is 1,494 km. Profile locations shown in Figure 1.

1247
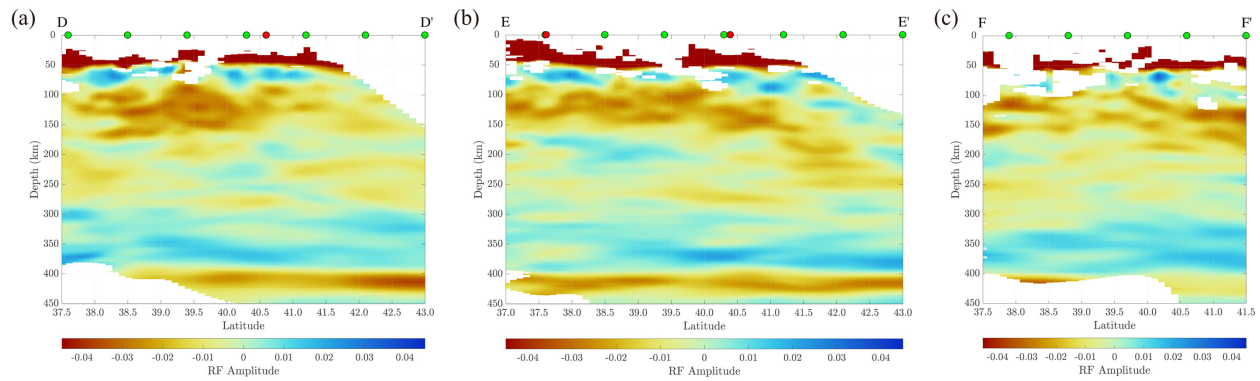
Figure 15. Sp CCP stack amplitudes on north-south oriented profiles D-D', E-E' and F-F'. Symbols and notations identical to Figure 11a, but horizontal axes are labeled with latitude. (a) Profile D-D' is located at 31.18°E, and the length of the profile is 612 km. (b) Profile E-E' is located at 37.35°E, and the length of the profile is 667 km. (c) Profile F-F' is located at 44°E, and the length of the profile is 445 km. Profile locations shown in Figure 1.

1253
1254
1255
1256
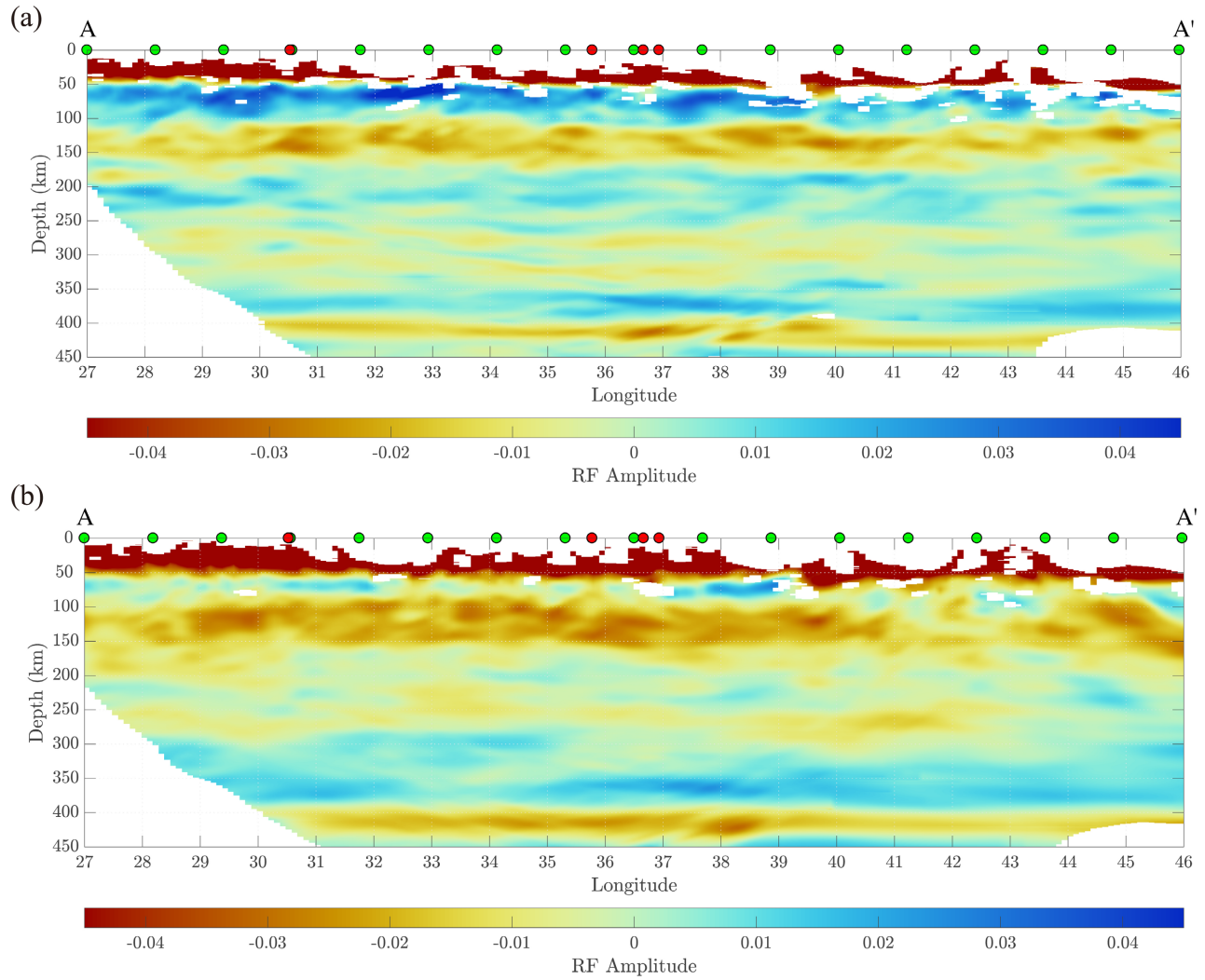
Figure 16. (a) Similar to Figure 11a but using a 2 to 20 s bandpass filter before deconvolution. Clear LAB phases are observed around ~70 km depth. (b) Similar to Figure 11a but using a 10 to 100 s bandpass filter.
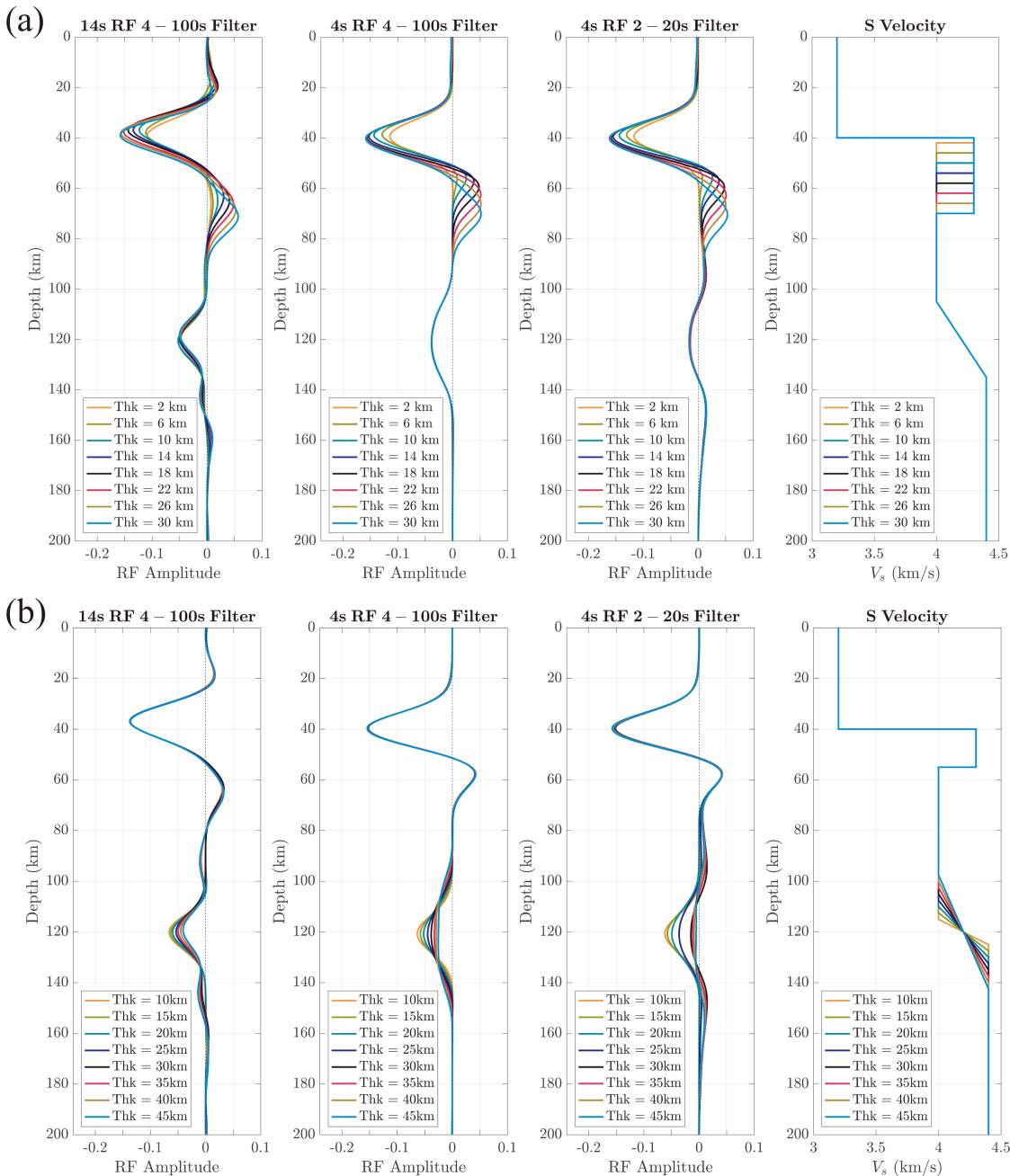
Figure 17. The frequency dependence of Sp receiver functions. (a) Synthetic Sp receiver functions for velocity models with varying mantle lithosphere thickness from 2 km to 30 km as indicated by the legend. The S waves have a ray parameter of 0.1098 s/km. Shear velocity structures are shown in the right-most panel and the mantle lithosphere is characterized by a high velocity layer starting from 40 km depth. The left-most panel shows receiver functions calculated from synthetic seismograms whose source-time functions are characterized by Gaussian first derivatives peaked at 14 s (~0.07 Hz). These waveforms were filtered with a 4 to 100 s bandpass filter before deconvolution. The middle-left panel is similar to the left-most one, but with source-time functions whose Gaussian first derivatives are peaked at 4 s (0.25 Hz). The middle-right

1272   panel is similar to the middle-left one, but with a 2 to 20 s bandpass filter. The LAB phase is

1273   larger amplitude for the cases where the source-time function has a 4 s period. (b) Sp receiver

1274   functions for structures where the positive velocity gradient at the base of the low velocity

1275   asthenosphere at 120 km has a varying depth extent. Velocity increases from 4.0 km/s to 4.4

1276   km/s within a layer as thin as 5 km to as broad as 45 km and, as indicated by the legend. The

1277   panels are arranged in the same way as in (a). Gradual positive velocity gradients (30-45 km

1278   depth extents) produce significant phases in seismograms with short-period (4 s) source-time

1279   function seismograms and the 4-100 s filter, but the amplitudes of these phases are reduced with

1280   the 2-20 s filter.

1281

1282

1283